On the Mach reflection of a solitary wave: revisited

WENWEN LI¹, HARRY YEH¹† AND YUJI KODAMA²

¹School of Civil and Construction Engineering, Oregon State University, Corvallis, OR 97331-3212, USA

²Department of Mathematics, Ohio State University, Columbus, OH 43210-1174, USA

Reflection of an obliquely incident solitary wave at a vertical wall is studied experimentally in the laboratory wave tank. Precision measurements of water-surface variations are achieved with the aid of laser-induced fluorescent (LIF) technique and detailed features of the Mach reflection are captured. During the development stage of the reflection process, the stem wave is not in the form of a Korteweg–de Vries (KdV) soliton but a forced wave, trailing by a continuously broadening depression. Evolution of stem-wave amplification is in good agreement with the Kadomtsev–Petviashvili (KP) theory. The asymptotic characteristics and behaviours are also in agreement with the theory of Miles (*J. Fluid Mech.*, vol. 79, 1977*b*, p. 171) except those in the neighbourhood of the transition between the Mach reflection and the regular reflection. The predicted maximum fourfold amplification of the stem wave is not realized in the laboratory environment. On the other hand, the laboratory observations are in excellent agreement with the previous numerical results of the higher-order model of Tanaka (*J. Fluid Mech.*, vol. 248, 1993, p. 637). The present laboratory study is the first to sensibly analyse validation of the theory; note that substantial discrepancies exist from previous (both numerical and laboratory) experimental studies. Agreement between experiments and theory can be partially attributed to the large-distance measurements that the precision laboratory apparatus is capable of. More important, to compare the laboratory results with theory, the corrected interaction parameter is derived from proper interpretation of the theory in consideration of the finite incident wave angle. Our laboratory data indicate that the maximum stem wave can reach higher than the maximum solitary wave height. The wave breaking near the wall results in the substantial increase in wave height and slope away from the wall.

Key words: pattern formation, solitary waves, waves/free-surface flows

---

1. Background

More than 50 years ago, Perroud (1957) studied reflection of solitary wave with oblique incidence along a vertical wall. He showed that the reflection pattern resembled the formation of a Mach stem that was known to exist for compressible shock waves

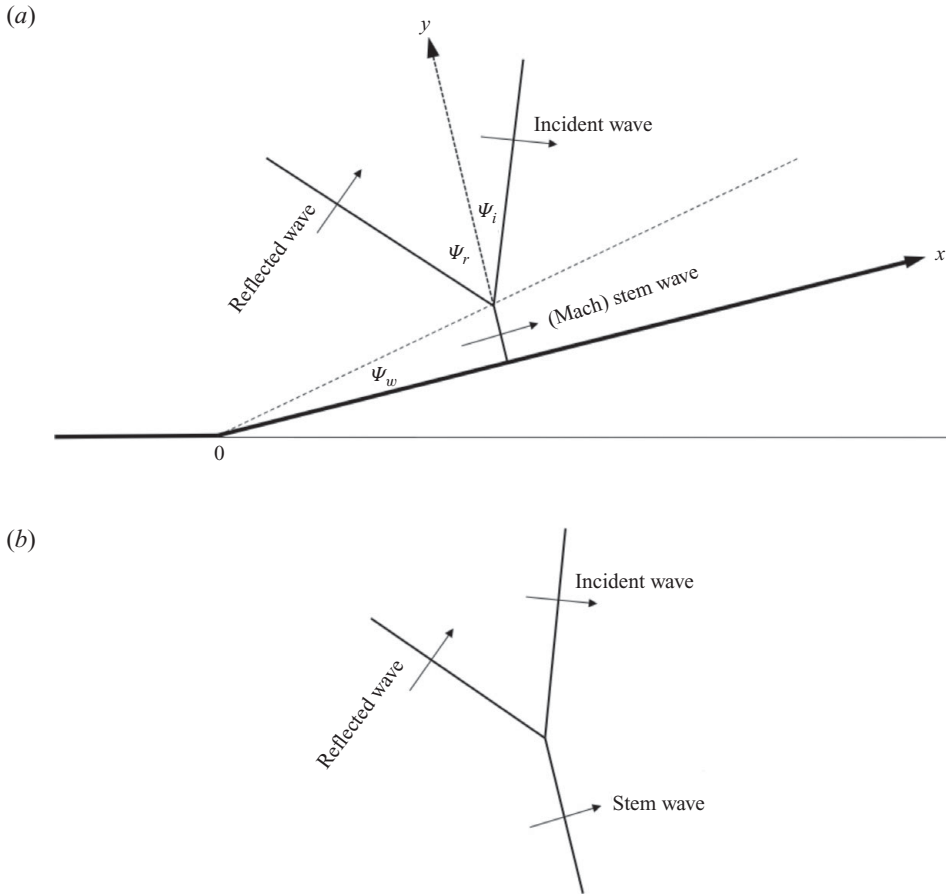† Email address for correspondence: harry@engr.orst.edu

FIGURE 1. Definition sketch for (*a*) Mach reflection and (*b*) three-wave resonant-interaction model by Miles (1977*b*): ψ_i, incident wave angle; ψ_r, reflected wave angle; ψ_w, angle of stem-wave development.

(e.g. von Neumann 1943; Courant & Friedrichs 1948). When a 'strong' shock impinges on a vertical wall with a small incident angle, a three-shock configuration emerges near the wall; they are the incident and reflected shock fronts, and the continuously growing 'Mach stem' forming perpendicular to the wall. The reflected shock front branches off from the incident shock away from the wall at the outer edge of the Mach stem (see the definition sketch in figure 1*a*). While the governing equations for compressible fluids are similar to the shallow-water wave equations, Perroud's experimental work (1957) – the realization of Mach reflection of solitary waves in the laboratory environment – is remarkable.

In his experiments, Perroud (1957) observed that the reflection pattern was regular (no stem formation) when the incident wave angle $\psi_i > 45°$; the Mach reflection pattern emerged when $20° < \psi_i < 45°$; no reflected wave appeared when $\psi_i < 20°$ but the stem length grew linearly with a constant stem angle ψ_w. The measured maximum amplification at the wall was $\alpha_w = a_w/a_i = 2.4$ when $\psi_i = 45°$ and $a_i = a_i^*/h_0 = 0.08$, where a_i^* is the incident wave amplitude and h_0 is the water depth at the quiescent state. Although his experiments were thorough, the results were not definitive owing

to the small-scale laboratory wave tank (6.1 m long, 1.1 m wide, 0.13 m deep with the water 4.0 and 6.0 cm depth), the imperfect wave generation (displacing a paddle driven by a weight with a pulley system) and measurement instruments (resistance-type wave gauges recording with a two-channel analogue oscillograph recorder). Those were however the best technology available at that time.

Hereinafter, unless stated otherwise, all the amplitude and length parameters are normalized with the quiescent water depth h_0. Wave amplification α is defined as the ratio of the wave amplitude to that of the incident wave, and the subscript i represents the incident wave; r represents the reflected wave; w represents the wave at the wall. The wave at the wall is termed the stem wave, because the Mach-stem-like feature appears in all the experimental results reported in this paper.

Inspired by Perroud's experimental findings, Miles (1977*b*) extended his theory for obliquely interacting multiple KdV solitons (1977*a*) to the Mach reflection problem. His theory considers shallow-but-finite water depth and small-but-finite wave amplitude to the lowest order (equivalent to the KdV limit). When the wave–wave interaction is weak, the amplification of two identical solitary waves intersecting each other at the angle $2\psi_i$ can be expressed as

$$\alpha_w = 2 + a_i \left(\frac{3}{2\sin^2 \psi_i} - 3 + 2\sin^2 \psi_i \right), \tag{1.1}$$

which holds only for $\sin^2 \psi_i \gg a_i$, and $a_i = O(\epsilon)$, where $\varepsilon \ll O(1)$. Equation (1.1) describes the condition equivalent to the maximum wave amplification α_w at a reflective wall when an incident wave with the amplitude a_i impinges on a rigid wall at an angle ψ_i. This type of interaction is termed as the 'non-grazing' reflection by Funakoshi (1980), and is similar to the 'non-glancing' reflection used for shock waves by von Neumann (1943).

Miles (1977*a*) further analysed the strong interaction case for the condition $\psi_i^2 = O(\varepsilon)$, and $a_i = O(\varepsilon)$, extending the methodology developed for unidirectional interaction of two KdV solitons by Whitham (1974). He found that no regular reflection of a solitary wave is possible when $0 < \psi_i^2 < 3a_i$. Assuming resonant triad interaction among three obliquely propagating KdV solitons as shown in figure 1(*b*), Miles (1977*b*) derived quantitative predictions for Mach reflection in the asymptotic state – the three waves are the incident, reflected and stem waves. He found that the stem-wave amplification is given by

$$\alpha_w = \begin{cases} \dfrac{4}{1 + \sqrt{1 - k^{-2}}}, & \text{for } k \geqslant 1, \\ (1+k)^2, & \text{for } k < 1, \end{cases} \tag{1.2}$$

where k is the interaction parameter:

$$k = \frac{\psi_i}{\sqrt{3a_i}}. \tag{1.3}$$

Note that the maximum amplification $\alpha_w = 4$ occurs at $k = 1$, and the reflection pattern is 'regular' when $k > 1$, and becomes that of Mach reflection when $k < 1$. The reflected wave amplification $\alpha_r (= a_r/a_i) \leqslant 1$ is

$$\alpha_r = \begin{cases} 1, & \text{for } k \geqslant 1, \\ k^2, & \text{for } k < 1, \end{cases} \tag{1.4}$$

the reflected wave angle is

$$\psi_r = \begin{cases} \psi_i, & \text{for } k \geqslant 1, \\ \sqrt{3a_i} > \psi_i, & \text{for } k < 1, \end{cases} \tag{1.5}$$

and the stem angle (or growth rate of the stem wave) is

$$\psi_w = \begin{cases} 0, & \text{for } k \geqslant 1, \\ \sqrt{\dfrac{a_i}{3}}\,(1-k), & \text{for } k < 1. \end{cases} \tag{1.6}$$

The foregoing theoretical predictions must be interpreted with caution. Miles's theory is based on the limit $\varepsilon \downarrow 0$ (weak nonlinearity), small oblique angles $\psi^2 = O(\varepsilon)$ and the resonant interaction taking place at the equilibrium state.

A few years later, Melville (1980) attempted to validate Miles's theory using a larger laboratory wave tank than that of Perroud (1957); Melville's wave tank was 18.3 m long, 6.2 m wide with the water at 20 and 30 cm depth. Solitary waves were generated along the 6.2 m long head wall and the waves were obliquely reflected from a vertical waveguide placed at the angles 10°–45° from the tank sidewall. The parameter $k = \psi_i / \sqrt{3a_i}$ was varied by changing the incident angle ψ_i but running two values of a_i (0.1 and 0.15). In spite of the use of a large wave tank, propagation distance of the Mach stem was limited due to the tank's finite breadth; maximum propagation distance along the oblique wall was limited to $x \leqslant 26.7$. Melville's experimental data showed that the maximum amplification at the wall α_w was 2.0 at $k = 1.43$, smaller than the observation of Perroud (1957) and one half the theoretical prediction of 4. Melville's data show that the measured amplification monotonically increases as the parameter k increases, and all the measured values were substantially lower than Miles's prediction (1.2). Melville demonstrated a trend that the growth angle ψ_w (see figure 1) approaches nil at the critical condition ($k = 1.0$) as predicted. He also found that the reflected amplitudes α_r were in fair agreement with the prediction, although the reflected wave angle ψ_r could not be identified due to the limited propagation distance ($x \leqslant 26.7$) – the reflected wave could not develop sufficiently given the short distance. Perhaps that is why the reflected wave profile was considerably different from that of a KdV soliton; the measured waveform was narrower than that of the soliton. Melville (1980) conjectured that the foregoing discrepancies must be related to the finite crest length of the reflected wave. He argued that while conservation of mass and energy determines the crest length of the reflected wave, conservation of momentum is violated near the offshore end of the reflected wave unless acceleration exists along the crest direction. Melville further pointed out that the critical condition at $k = 1.0$ means a vanishing stem length; hence, the resonant model based on an infinite extent breaks down (the model shown in figure 1b): i.e. the no-flux boundary condition at the wall cannot be modelled with Miles's three-wave resonant interaction.

Almost at the same time as Melville's laboratory study, Funakoshi (1980) conducted numerical experiments to verify Miles's theoretical predictions. It is not surprising that Funakoshi's numerical results are in good agreement with the theory because the governing equations are the same as Miles's limits (KdV approximation). For $k > 1$, the numerical results agree better with the results for a non-grazing reflection (1.1). No stationary state could be attained for $k \approx 1.0$, which is attributed to the limitation of numerical work. Consequently, he could not numerically demonstrate the critical amplification of $\alpha_w = 4.0$ at $k = 1.0$. Funakoshi presented the results for $a_i = 0.05$ with

$\psi_i = 2.25°-30°$, and commented that it takes a very long time to achieve the stationary Mach-reflection pattern.

Unlike Funakoshi (1980) and others (e.g. Kato, Takagi & Kawahara 1998) whose numerical models are the same order of approximation as the theory by Miles (1977a,b), numerical experiments of Tanaka (1993) were based on the higher-order spectral method. This higher-order model allowed him to study conditions less restricted in the nonlinearity parameter a_i and the incident wave angle ψ_i. As in numerical experiments of Funakoshi (1980), Tanaka found that it requires long propagation to achieve the saturated conditions in stem amplitude ($x \sim 100-300$). However, his model also failed to simulate the fourfold amplification of the stem wave predicted by (1.2). The simulated maximum stem-wave amplification was $\alpha_w = 2.897$ at $k = 0.695$ in the case of $a_i = 0.3$. When $k > 0.695$, Tanaka's numerical results are in better agreement with the prediction for non-grazing reflection (1.1) than the prediction for strong resonant interaction (1.2). Tanaka (1993) commented that the Mach-stem amplitude becomes higher ($a_w = 0.905$) than the highest two-dimensional solitary wave ($a = 0.827$; cf. Longuet-Higgins & Fenton 1974). A similar numerical study was conducted by Barakhnin & Khakimzyanov (1999) and it was found that the values of ψ_r, ψ_w and α_r are well predicted by Miles's theory with small amplitude, $a_i = 0.05$, but not stem amplification, α_w.

Recently, Kodama, Oikawa & Tsuji (2009) have derived asymptotic solutions for the Kadomtsev–Petviashvili (KP) equation for symmetric initial waves made of four semi-infinite line solitons: Chakravarty & Kodama (2009) called the (3142)-type and the O-type solutions which correspond to the Mach reflection and the regular reflection, respectively. Their results successfully reproduced Miles's theoretical predictions (1.2), which demonstrates that Miles's resonant interaction is equivalent to the asymptotic solution to the initial-value problem of the KP equation. Kodama *et al.* (2009) demonstrated that their solution recipe is capable of describing the development stage of the reflection although the reflected wave characteristics far away from the reflection wall must be given *a priori*.

2. On incident wave angle ψ_i

According to the foregoing background review, Miles's theoretical predictions (1.2)–(1.6) are generally supported by numerical simulations of the models with the same limits and assumptions $a_i = O(\varepsilon)$ (weak nonlinearity) and small oblique angles $\psi^2 = O(\varepsilon)$. On the other hand, previous laboratory experiments failed to verify Miles's theory, and so did the higher-order numerical simulations by Tanaka (1993) and Barakhnin & Khakimzyanov (1999); the observed or simulated features and behaviours do not match the theoretical predictions.

When we compare laboratory and numerical results with the theory, one problem is the assumption of a small oblique angle of incident wave ψ_i. Recall that experiments of Perroud (1957) were performed with $\psi_i = 0.35-0.79$ rad ($20°-45°$), those of Melville (1980) were performed with $\psi_i = 0.17-0.79$ rad ($10°-45°$), numerical experiments of Funakoshi (1980) with $\psi_i = 0.04-0.52$ rad ($2.25°-30°$) and numerics of Tanaka (1993) were performed with $\psi_i = 0.17-1.05$ rad ($10°-60°$). The condition $\psi^2 = O(\varepsilon)$ imposed by Miles (1977b) was clearly violated for a majority of the previous experiments, which must be a reason why some of the previous experimental data for $k > 1.0$ (Funakoshi 1980; Tanaka 1993) agree better with the results of non-grazing reflection (1.1) that is valid for $\sin^2 \psi_i \gg a_i$.

Recently, Yeh, Li & Kodama (2010) have shown the treatment of the oblique incident angle ψ_i in the KP equation. Note that the KP equation is equivalent to Miles's theory, assuming shallow-but-finite water depth, small-but-finite wave amplitude to the lowest order and a small oblique angle. More explicitly, the assumptions in the KP equation are $a_0/h_0 = O(\varepsilon)$, $(h_0/\lambda_0)^2 = O(\varepsilon)$ and $\tan^2 \psi_i = O(\varepsilon)$, in which h_0 is the water-depth scale, a_0 and λ_0 are the scales of wave amplitude and length, respectively, and $\varepsilon \ll O(1)$. It is important to point out, however, subtle difference in the KP theory from Miles's theory. The form of the small-but-finite angle, $\tan^2 \psi_i = O(\varepsilon)$, arises systematically in the derivation process of the KP equation from the Euler formulation, whereas Miles (1977b) assumed $\psi^2 = O(\varepsilon)$ – but not $\tan^2 \psi_i$ – from the outset of his analysis.

The KP equation in terms of the water-surface elevation η from the equilibrium state can be written in the dimensional form:

$$\left(\eta_t + c_0 \eta_x + \frac{3c_0}{2h_0} \eta \eta_x + \frac{c_0 h_0^2}{6} \eta_{xxx} \right)_x + \frac{c_0}{2} \eta_{yy} = 0, \tag{2.1}$$

where $c_0 = \sqrt{g h_0}$, the x-direction represents the primary wave propagation, and the weak transverse perturbation is in the y-direction. An exact solution to (2.1) is

$$\eta = a_0 \operatorname{sech}^2 \left[\sqrt{\frac{3 a_0}{4 h_0^3}} \left\{ x + y \tan \psi - c_0 \left(1 + \frac{1}{2} \frac{a_0}{h_0} + \frac{1}{2} \tan^2 \psi \right) t \right\} \right]. \tag{2.2}$$

While (2.2) resembles the form of a solitary wave, it does not represent the KdV soliton unless $\psi = 0$. The solution is not invariant to coordinate orientation: a line soliton in the x-direction cannot maintain its identity by rotating the coordinate system. Consider a single and isolated KdV soliton. At a given location (x, y), the temporal profile of (2.2) becomes narrower as $|\psi|$ increases, which is evidently physically unrealistic and is a shortcoming of the 'exact' solution (2.2). It is emphasized that the incident wave in the present problem is in the form of a KdV soliton, but not the distorted waveform of (2.2). To remedy this problem, (2.2) is arranged to

$$\eta = a_0 \operatorname{sech}^2 \left[\sqrt{\frac{3 a_0}{4 h_0^3 \cos^2 \psi}} \left\{ x \cos \psi + y \sin \psi - c_0 \cos \psi \left(1 + \frac{1}{2} \frac{a_0}{h_0} + \frac{1}{2} \tan^2 \psi \right) t \right\} \right]. \tag{2.3}$$

Taking the propagation direction of a line soliton to be $\xi = x \cos \psi + y \sin \psi$, and expanding $\cos \psi$ in the last term by $\cos \psi = 1 - \frac{1}{2} \tan^2 \psi + O(\varepsilon^2)$, yield

$$\eta = a_0 \operatorname{sech}^2 \left[\sqrt{\frac{3 a_0}{4 h_0^3 \cos^2 \psi}} \left\{ \xi - c_0 \left(1 + \frac{1}{2} \frac{a_0}{h_0} \right) t + O(\varepsilon^2) \right\} \right]. \tag{2.4}$$

Defining the amplitude $\hat{a}_0 = a_0 / \cos^2 \psi = a_0(1 + \tan^2 \psi) = a_0(1 + O(\varepsilon))$, we have the KdV soliton in the ξ-direction:

$$\hat{\eta} = \hat{a}_0 \operatorname{sech}^2 \left[\sqrt{\frac{3 \hat{a}_0}{4 h_0^3}} \left\{ \xi - c_0 \left(1 + \frac{1}{2} \frac{\hat{a}_0}{h_0} \right) t \right\} \right] + O(\varepsilon). \tag{2.5}$$

This procedure results in the higher-order correction to the small angle approximation. The amplitude $\hat{a}_0$ now represents the physical wave amplitude realized in the laboratory. While (2.5) is no longer the exact solution to the KP equation (2.1),

it still remains valid within the KP limit: error caused by (2.5) would be the higher order for (2.1).

Kodama *et al.* (2009) studied symmetric V-shape initial waves that are formed by two identical semi-infinite line solitons – note that this condition is equivalent to the Mach reflection problem in the half-plane. They considered the KP equation in the following form:

$$(4u_T + 6uu_X + u_{XXX})_X + 3u_{YY} = 0. \tag{2.6}$$

This equation can be obtained by scaling (2.1) with

$$u = \frac{3}{2}\frac{\eta}{h_0}, \quad X = \frac{x}{h_0} - \frac{c_0}{h_0}t, \quad Y = \frac{y}{h_0}, \quad T = \frac{2}{3}\frac{c_0}{h_0}t. \tag{2.7}$$

The exact solution of the line soliton is found to be

$$u = A_0 \, \text{sech}^2 \left[\sqrt{\frac{A_0}{2}}(X + Y\tan\psi - CT) \right], \tag{2.8}$$

where $C = \frac{1}{2}A_0 + \frac{3}{4}\tan^2\psi$. Kodama *et al.* (2009) derived for the asymptotic stem-wave amplification that turned out identical to (1.2), and they identified the critical condition at $\tan\psi = \sqrt{2A_0}$, which appears similar to $k = 1.0$ in (1.3). Because the amplitude A_0 can be expressed with the physical wave amplitude $\hat{a}_0$ by

$$A_0 = \frac{3}{2}\frac{a_0}{h_0} = \frac{3}{2}\frac{\hat{a}_0\cos^2\psi}{h_0}, \tag{2.9}$$

the interaction parameter of the KP theory can be expressed as

$$\kappa = \frac{\tan\psi_i}{\sqrt{3\,a_i}\cos\psi_i}. \tag{2.10}$$

It is important to recognize that, instead of the interaction parameter $k = \psi_i/\sqrt{3a_i}$, the parameter κ of (2.10), which has more proper form of the small incident wave angle ψ_i, should be used in (1.2) and (1.4)–(1.6), when the theory is compared with the experiments involving small-but-finite values of the incident wave angle ψ_i.

With the corrected parameter (2.10), figure 2 demonstrates substantial improvement when comparing numerical results of Tanaka (1993) with the theoretical prediction of (1.2). Tanaka's model is based on higher-order approximation, and the simulations were made for finite amplitude waves with $a_i = 0.3$. In his paper, Tanaka drew a conclusion that the transition from Mach reflection to regular reflection happens at $k = 0.695 < 1$ with the maximum amplification $\alpha_w = 2.897$, and that the data with $k > 0.695$ are in better agreement with Miles's theory for non-grazing reflection (1.1) than the resonant interaction model (1.2). Such original conclusions are no longer true when the modified interaction parameter (2.10) is used instead of the original (1.3). The maximum amplification of his numerical experiments is now at $\kappa = 1.03$, and his results are in good agreement with the theory except for the cases near $\kappa \sim 1.0$, where the theoretical four fold amplification could not be achieved by the numerical simulation. His results remain in better agreement with (1.1) only when the value of κ is very large as anticipated.

3. Laboratory experiments

Laboratory experiments were performed in a wave tank designed and constructed for long-wave research (see figure 3). The wave tank (7.3 m long, 3.6 m wide and
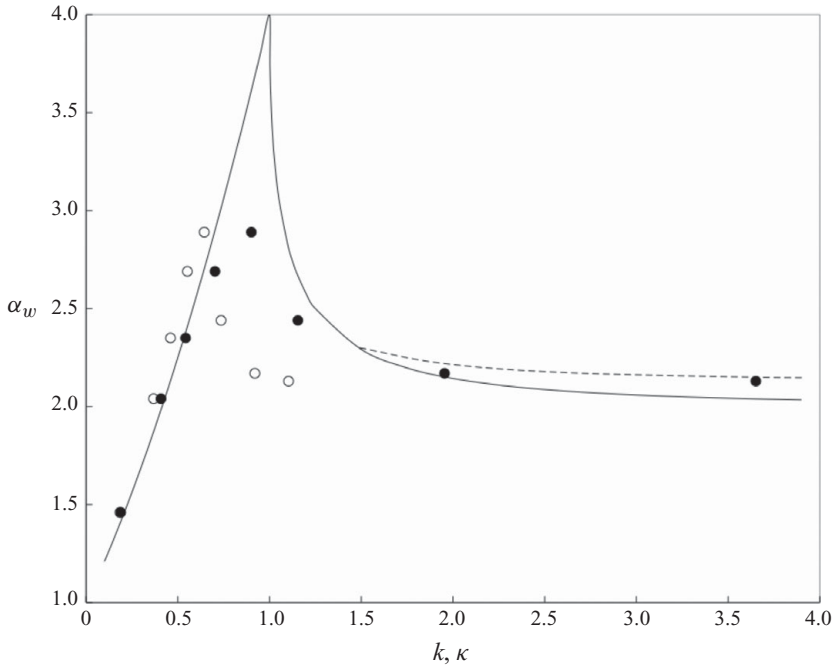
Figure 2. Comparison of numerical data of Tanaka (1993) with prediction of Miles (1977b). The numerical data are marked $\circ$ with the original interaction parameter $k = \psi_i/\sqrt{3a_i}$, and $\bullet$ with the modified parameter $\kappa = \tan\psi_i/(\cos\psi_i\sqrt{3a_i})$; ——, (1.2); ------, (1.1).

0.30 m deep) is elevated 1.2 m above the laboratory floor; the bottom and sidewalls are made of 12.7 mm thick glass plates. Prior to assemblage, the top surface of the entire $3.6\,\text{m} \times 7.3\,\text{m}$ aluminium frame was planed in one piece to achieve a smooth flat surface, which, together with the height-adjustable base columns, enables us to place glass plates directly on the frame precisely in a horizontal plane.

The wave basin is equipped with a 16-axis directional wavemaker system along the 3.6 m long headwall, capable of generating arbitrarily shaped, multi-directional waves. Each wave paddle is pushed through hinge connections by two adjacent linear-motor motion devices. Compared with traditional rotary motors, linear motors are inherently more accurate for producing linear positioning. A push rod at one edge of a paddle is connected directly to the carriage of the unit. The paddles are made of PVDF (polyvinylidene fluoride) plates that are driven horizontally in piston-like motions. Each paddle has a maximum horizontal stoke of 55 cm – more than adequate to generate very long waves with a water depth of 6.0 cm in our experiments. This precision wavemaker system, together with the precise wave tank, is needed to investigate nonlinear dynamics of long-wave motion.

While the wavemaker system is capable of generating arbitrarily shaped, multi-directional waves, we chose to generate a solitary wave in the normal direction (along the sidewalls). An obliquely incident solitary wave was created by placing a 2.54 cm thick Plexiglas vertical wall at a prescribed azimuth angle from the tank's sidewall (see figure 3); this is the same set-up as both Perroud (1957) and Melville (1980) adopted in their laboratory experiments. Because the wave paddles are driven synchronously along the sidewalls, any ambiguity associated with potential deviation caused by the paddle deformation is eliminated. Solitary waves are generated using
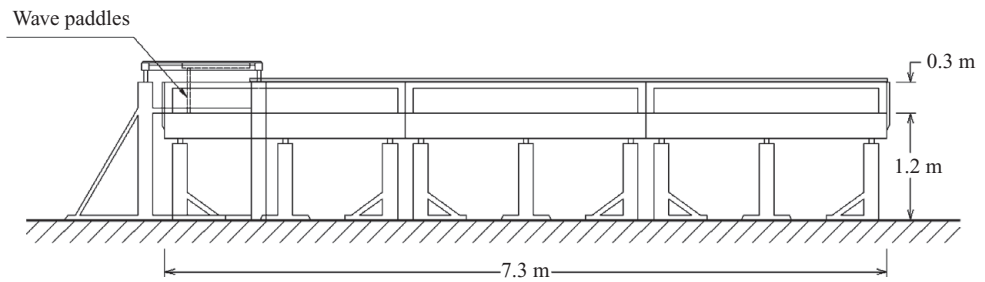
(*a*)
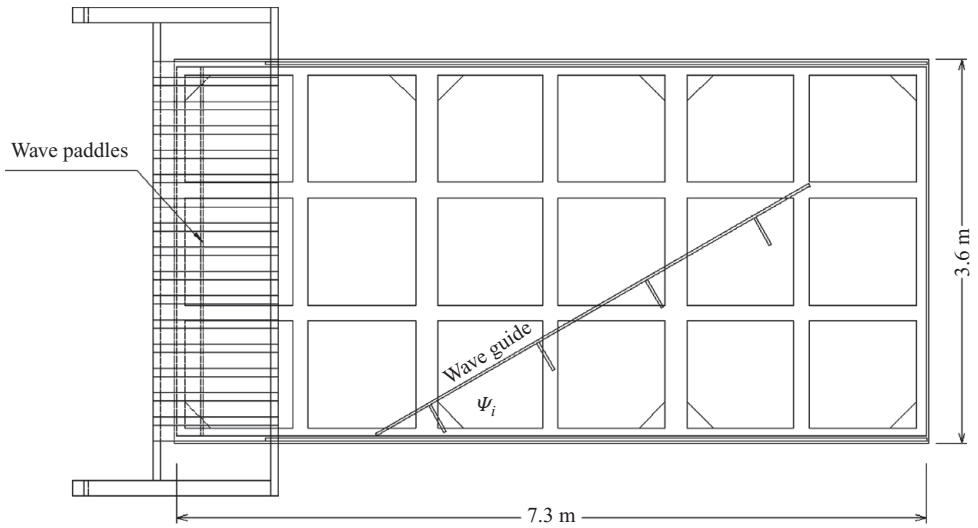
(*b*)

FIGURE 3. Schematic drawings of the laboratory apparatus: (*a*) a plan view showing the waveguide that creates an oblique wave reflection and the tank frame that can be seen through the bed that is made of glass plates; (*b*) an elevation view.

the algorithm developed by Goring (1979), which is based on KdV solitons. Slightly more stable solitons could be generated using the higher-order solutions (Guizien & Barthélemy 2002). The KdV soliton is used so that our laboratory measurements are consistent with the KdV and KP theories. Identifying deviations resulting from the mathematical assumptions and approximations is one of our objectives. Note that the generated waves are precisely replicable with the maximum error being less than 0.06 mm (or 0.1 % of the depth) for a solitary wave with the amplitude $a_i^* = 1.73$ cm in $h_0 = 6.0$ cm. (Hereinafter, dimensional quantities are denoted by an asterisk.) The imperfect trailing portion of the generated solitary waves shown in figure 4 is due to the approximation of the KdV soliton.

The size of the wave basin used by Melville (1980) was 18.3 m × 6.2 m, which is physically larger than the present apparatus. Melville stated in his paper, however: 'the large scale of the basin made it difficult to prevent draughts in the laboratory from generating surface waves'. On the other hand, our laboratory condition was carefully controlled, which allowed us to perform the experiments in the depth $h_0 = 6.0$ cm, which is shallower than Melville's $h_0 = 20.0$ and 30.0 cm. As a result, the present apparatus is considered to be effectively larger in terms of the non-dimensionalized domain than Melville's wave basin.
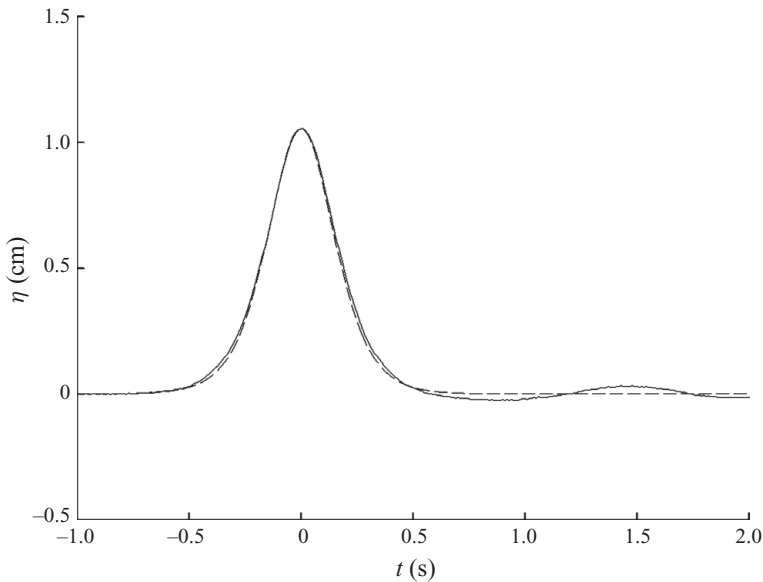
FIGURE 4. Typical profile of the generated KdV soliton (solid line) at $x^* = 543$ cm with the water depth of $h_0 = 6.0$ cm, and the dashed line represents the profile of the KdV soliton. The slightly wider profile and the formation of a small trailing dispersive wavetrain are due to the KdV approximation used in the generation algorithm.

To examine temporal and spatial variations of water-surface profiles, we used the laser-induced fluorescent (LIF) method. The LIF method has been used to record water-surface variations as early as 1980s (Yeh & Ghazali 1986; Ramsden 1993; Duncan *et al.* 1994), and has significantly improved accuracy due to recent advances in optical devices (e.g. Duncan *et al.* 1999; Gardarsson & Yeh 2007; Diorio, Liu & Duncan 2009). Figure 5 shows a set-up of the LIF method used in this study. A laser beam (a 5 W diode-pumped solid-state laser mounted on the traversable carriage) is converted to a thin laser sheet using a cylindrical lens. Two front-surface mirrors direct the laser sheet to illuminate the vertical plane perpendicular to the wall. With the aid of fluorescein dye dissolved in water, the vertical laser-sheet illumination from above induces the dyed water to fluoresce and identifies the water-surface directly and non-intrusively.

The bright horizontal strip shown in figure 5 is the illuminated water dyed with fluorescein. The bright vertical line in the figure is the reflection of the laser sheet from the Plexiglas vertical waveguide. As the wave passes through the light sheet the illuminated profiles are recorded by a high-speed high-resolution video camera (1280×1024 pixels and 30–500 frames per second) that is set 120 cm away from the plane of the illuminated laser light sheet. Prior to each set of experiments, the illuminated plane was calibrated with a target image. The captured images are rectified and processed with the calibrated image so that the resulting images can be analysed quantitatively. It is emphasized that the transparent glass bed of the tank minimizes the reflection of laser illumination that could have caused contamination in the image analysis for the wave profiles. To identify the air–water interface, we traced image pixels in the vertical direction from top to bottom; the interface was determined where the gradient of the light intensity reaches a maximum. A similar procedure was used by Liu & Duncan (2006) for their laboratory experiments on wave-breaking processes.
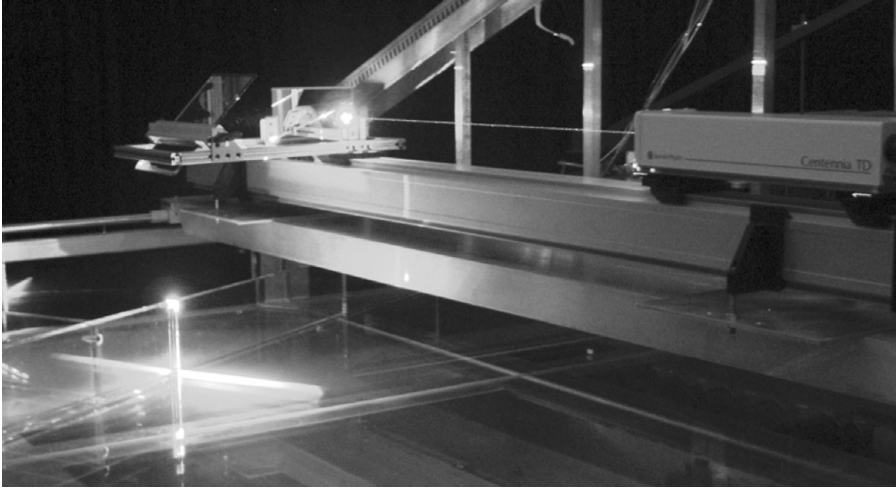
FIGURE 5. Set-up of the LIF method, composed of the 5 W laser, the cylindrical lens and two front-surface mirrors. The water dyed with fluorescein fluoresces when excited by the laser sheet.

One of the difficulties associated with the LIF method for measuring long waves is the limitation in resolution. Unlike the experiments for capillary waves or breaking waves, long waves have an inherently small vertical-to-horizontal length-scale ratio. This causes insufficient resolution in the vertical direction even when the $1280H \times 1024V$ pixel camera is used. Our laboratory experiments of Mach reflection require measurements of small wave amplitudes (a few centimetres) in a large horizontal span (more than 75 cm). To circumvent this difficulty, we repeat LIF water-surface profiles on approximately 27 cm segments, and make a montage of the three-segment profiles to cover the 80 cm long transect perpendicular to the wall. This procedure is only possible with a laboratory apparatus that is capable of precise replication. A typical example of the resulting wave profiles is shown in figure 6. Because the LIF method permits measuring water-surface elevations non-intrusively, any uncertainty caused by meniscus contamination in the measurement often associated with wave gauges can be avoided. In fact, the LIF method is capable of capturing the meniscus effect on the wall as shown in figure 6: see the small curvature of the profile at the wall ($y = 0$). The concave curvature of meniscus at the wall is present prior to the run-up on the vertical waveguide. The meniscus flips to its convex form during the run-up. The capillary rise on the Plexiglas wall varies from approximately 1 to 1.5 mm, depending on contamination of the water and the wall surface. In spite of a large variation in capillary rise, the meniscus effect is limited close to the wall, $y^* < 1$ cm, and does not affect the rest of the profiles. Hence, hereinafter, the data will be presented without showing the meniscus, plotting the profile from $y^* = 1.27$ cm (or $y = 0.21$). A careful observation of figure 6 reveals negligibly minute mismatches in the profiles near $y^* = 25$ and 50 cm; these mismatches are due to an imperfect montage process.

To identify energy decay of the solitary wave, the e-folding distance of amplitude attenuation was measured at four different transverse locations without installing the oblique reflective wall for $a_i = 0.076$–0.55 with the water depth $h_0 = 6.0$ cm. It was found that the amplitude decays slowly – the average e-folding distance being 55.5 m (or the exponential decay rate 0.018 m^{-1}). Hence, it appears that viscous effect in
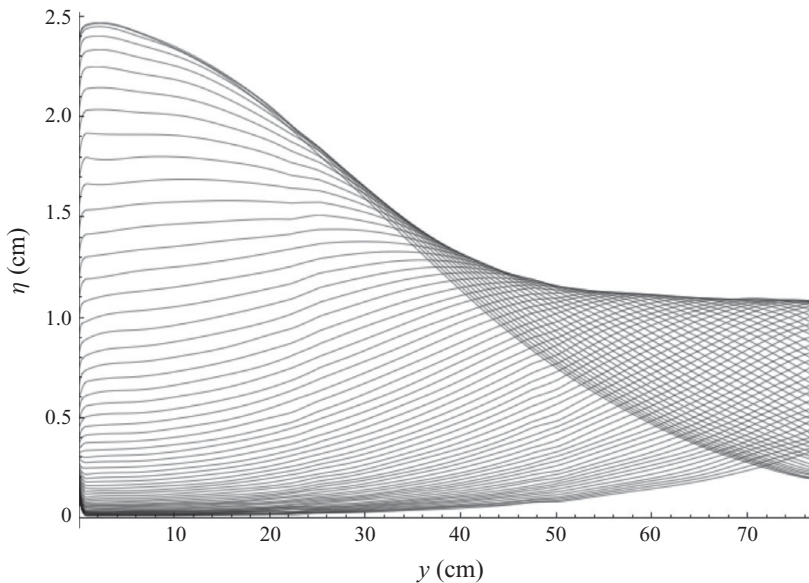
FIGURE 6. Temporal variation of the water surface profile along the transect perpendicular to the oblique wall at $x^* = 427$ cm with the incident wave angle $\psi_i = 30°$ and the water depth of $h_0 = 6.0$ cm. The profiles were constructed by making a montage of three LIF images. The time interval of each profile is $1/100$ s. Note the meniscus effect at the wall.

the present experiments is not negligible, but sufficiently small to examine the Mach reflection phenomenon.

One of the shortcomings of the laboratory experiments is the limitation of wave-propagation distance: physical size of the apparatus prevents the observations of a long-distance wave evolution. To circumvent this, we extend the experiment by generating the waveform measured at the furthest location observed in the previous run. In other words, the effectively larger wave tank is achieved by patching the two experimental runs: the original 'parent' experimental run and the subsequent 'extended' run. Unlike the parent experimental run, in which only an incident solitary wave was generated, the two-dimensional (2D) waveform including the reflected and stem waves needs to be generated for the extended run. This practice is made possible because the present wavemaker system is capable of replication of the 2D waveform.

When the incident wave is generated to propagate parallel to tank's sidewall (in the normal direction), the reflected wave has a large propagation angle, see figure 1(*a*). For example, when the incident wave angle is $\psi_i = 30°$, the reflected wave angle would be approximately $\psi_r = 40°$. Therefore, for the extended experimental run, the reflected wave must be re-created with the angle of $70°$ relative to the wave paddles. Waves with such a large oblique angle would be difficult to generate even with our wavemaker system. Consequently, for the extended run, the incident wave is generated with the oblique angle to form the stem wave along the sidewall, instead of the obliquely placed waveguide. In other words, the incident wave is generated along the waveguide (see figure 3*a*). In this manner, when the incident wave angle is $\psi_i = 30°$, the reflected wave can be comfortably generated with the prescribed oblique angle of, say, $40°$, but not $70°$. It is cautioned that this patching procedure to effectively extend the laboratory tank induces some error because it is not possible to perfectly reproduce the wave measured in the parent experimental run with the

16-axis wavemaker system. Nonetheless, the data that will be discussed in the next section reasonably demonstrate continuous transition from the parent experimental run to the corresponding extended run.

4. Results

For all results presented in this paper, the origin of coordinates is taken at the edge of the oblique vertical wall as shown in figure 1; the x-direction points horizontally along the wall, y-direction points perpendicularly away from the wall and z-direction points upwards. As we stated earlier, the wave along the wall is termed the stem wave, because the Mach-stem-like feature is present in all of the experiments reported herein. Unless otherwise stated, all the parameters are normalized with the quiescent water depth h_0, and the time scale $\sqrt{h_0/g}$, where g is the gravitational acceleration. The amplification of the stem wave α_w is defined as the ratio of wave amplitude at the wall (or more precisely at $y = 0.21$ to avoid the meniscus effect) to the incident wave amplitude measured offshore at the same longitudinal (x) location: $\alpha_w = a_w/a_i$. The reflected-wave amplification is presented in the same manner, $\alpha_r = a_r/a_i$. The subscripts i, w, and r denote the quantity for the incident, stem and reflected waves, respectively. The incident wave amplitude a_i measured at $x = 10.2$ and the values of the interaction parameter κ are used to identify the experimental run. Note that due to viscous attenuation, both a_i and κ vary in the propagation.

Primary references used in this study are theoretical predictions of Miles (1977b), laboratory data of Melville (1980) and numerical experiments of Tanaka (1993). In addition, our laboratory results are compared with our numerical calculation based on the KP equation (2.1). As discussed earlier, when the laboratory results are compared with the theory, the modified interaction parameter κ presented in (2.10) should be used, instead of k in (1.3). The present experiments focus on the conditions of the quiescent water depth $h_0 = 6.0$ cm and the incident wave angles $\psi_i = 20°$, $30°$ and $40°$. Our objectives are to realize the Mach reflection phenomenon in the laboratory environment, to provide an accurate anatomy of Mach reflection formation and to analyse the results with the previous laboratory observations (cf. Melville 1980), numerical predictions (cf. Tanaka 1993) and the theoretical predictions (Miles 1977a,b), as well as our numerical simulations based on the KP equation.

4.1. Water-surface profiles

Compiling three LIF segments of the water-surface profiles in the y-direction yields a montage of water-surface maps in the y–t plane with adequate coverage, $0 < y < 13.0$, as shown in figure 7. The figure shows the wave profile at $x = 71.1$ for the case $a_i = 0.188$ with the oblique wall (or equivalently the incident wave angle) $\psi_i = 30°$. The interaction parameter at $x = 71.1$ is $\kappa = 0.918 < 1$; hence, the condition should form a Mach reflection according to (1.2)–(1.6). (Note that $\kappa = 0.888$ at $x = 10.2$; the slight increase in κ at $x = 71.1$ is due to the amplitude attenuation.) The plot in figure 7 is made from 150 slices of spatial profiles – 100 slices per second – with approximately 3000 pixel resolution in the y-direction. As expected, the formation of Mach stem is realized, in which the apices of the incident and reflected waves separate away from the wall by the third wave that perpendicularly intersects the wall. Figure 7 shows that the reflected wave amplitude is smaller than that of the incident wave as anticipated for the Mach reflection. Small wavelets emanating from the wall (generated near the cessation of the rundown process) and trailing the Mach stem are gravity–capillary waves (ripples) with a wave period of approximately 0.2 s.
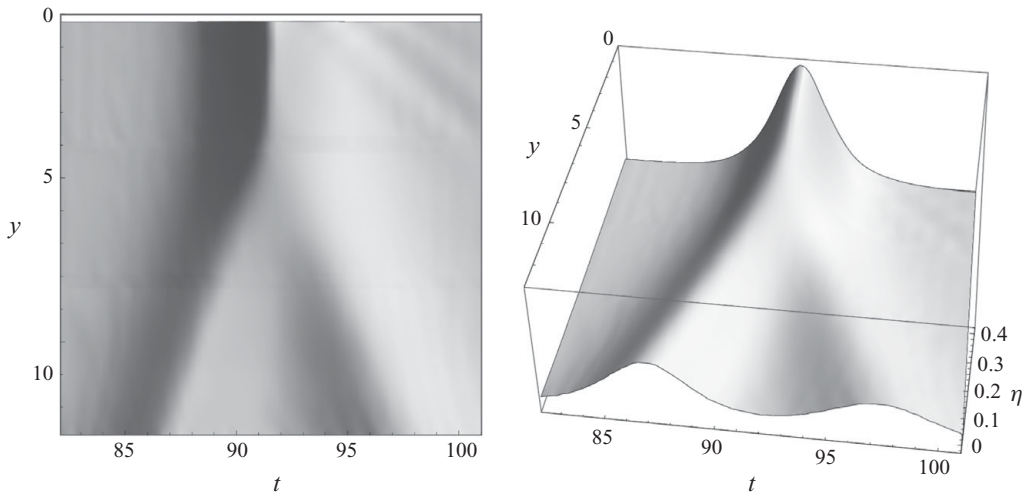
FIGURE 7. Two views of the temporal variation of the water-surface profile in the y-direction (perpendicular to the wall) at $x = 71.1$: the wall is located at $y = 0$, the water depth $h_0 = 6.0$ cm, the incident wave amplitude $a_i = 0.188$ and the angle $\psi_i = 30°$ ($\kappa = 0.888$). The data were obtained by the LIF method with the vertical laser sheet along the y-direction. See the stem formation along the wall ($y = 0$) and the difference in angle and amplitude in the y–t plane between the incident and reflected waves.

The air–water–wall contact line must have created a gravity–capillary disturbance due to the motion of the surface curvature with small radii. Note that the water surface in our laboratory is likely to be contaminated by soluble surfactants typically found in the bulk water and ambient airborne dust; hence, the surface tension is probably lower than 74 dyn cm^{-1} (surface tension was not measured).

Taking advantage of the LIF method of directly capturing the water-surface profile, the reflected wave angle and the stem length are measured unambiguously. The loci of the maximum water elevation (i.e. wave crest) of the incident wave, the stem and reflected wave are shown in figure 8 for the same waves as presented in figure 7. Using the (measured) phase speed, the reflected wave angle ψ_r is calculated and found to be $\psi_r = 41.6°$. Evidently, $\psi_i \,(= 30°) < \psi_r$, one of the characteristics of Mach reflection. Near the offshore end $y > 10$, the wave reflection at the wall does not affect the incident wave that forms a straight crest line with uniform amplitude; the crest line of the reflected wave also becomes straight with uniform amplitude but only where x is sufficiently large, say $x \geqslant 30.5$. The stem crest length is determined at the intersection of the linear extension of the incident-wave crest line from offshore (see figure 8): we matched the crest-line slope in the y–t plane with the measured incident wave speed. Unlike the theoretical model (figure 1), our laboratory data found that the extension of the reflected-wave crest line intersects slightly offshore with the stem-wave crest line. Such a direct and detailed measurement of Mach stem length was not possible in the previous laboratory experiments that used wave-gauge measurements. Melville (1980) estimated the stem length by computing the wave-phase deviation based on the correlation function between wave-gauges aligned normal to the wall. His procedure was necessary because of noise present in his laboratory and the difficulty in identifying the wave phase from the wave-gauge data at discrete locations.
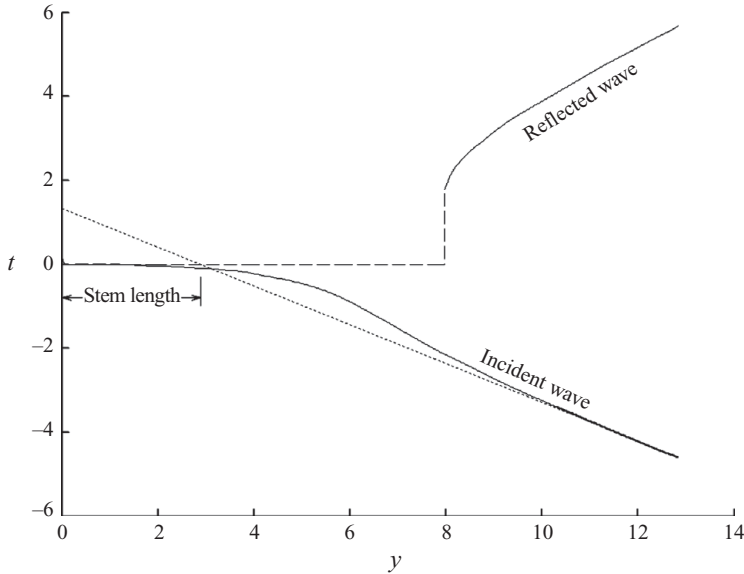
FIGURE 8. Loci of the maximum water-surface elevations, i.e. wave crests, identified from the wave profile shown in figure 7. The intersection of the linearly extended crest of the incident wave to the Mach stem determines the stem length.

Figure 9 presents temporal variations of the stem-wave profile at the wall ($y = 0.21$) and the offshore water-surface profile (at $y = 12.5$) for the same wave as shown in figures 7 and 8. Also plotted are the KdV-soliton profiles fitted to the measured wave amplitudes. The incident and reflected waves are sufficiently but not completely separated from each other at $y = 12.5$. The wave amplitude of the reflected wave is evidently smaller than that of the incident wave: the amplification is $\alpha_r = 0.634$. Both incident and reflected waveforms exhibit the form of the KdV soliton. However, the lee portion of the reflected wave profile sags down faster than the soliton profile and it does not approach the quiescent water level but further dips to the negative water level. Melville (1980) pointed out that the observed reflected wave was narrower than that of the solitary wave; the deviation he observed was greater than that shown in figure 9. The larger discrepancy in Melville's data can be attributed to the short distance of his measurements (at $x = 16.7$), where the reflective wave was still under development and losing its energy along the crest via diffraction. On the other hand, the profile in figure 9 was taken further downstream at $x = 71.1$, although it is still at the development stage, which will be discussed later.

The stem wave at the wall shown in figure 9(a) does not form the profile of a KdV soliton. While the wave profile is symmetric, the wave breadth is broader than that of the soliton. This characteristic is consistent for all the experiments we performed as well as consistent with the measurements made by Perroud (1957) and Melville (1980). A trailing depression is apparent in figure 9(a); the depression formation behind the stem wave was also pointed out in the previous laboratory studies by Perroud (1957) and Melville (1980). Examination of the numerical results by Tanaka (1993, figure 15) shows a similar depression formation in the early stage of the simulation. In his numerical calculations, Funakoshi (1980) numerically observed the trough depth increasing and subsequently decreasing slowly until vanishing at $t \to \infty$.
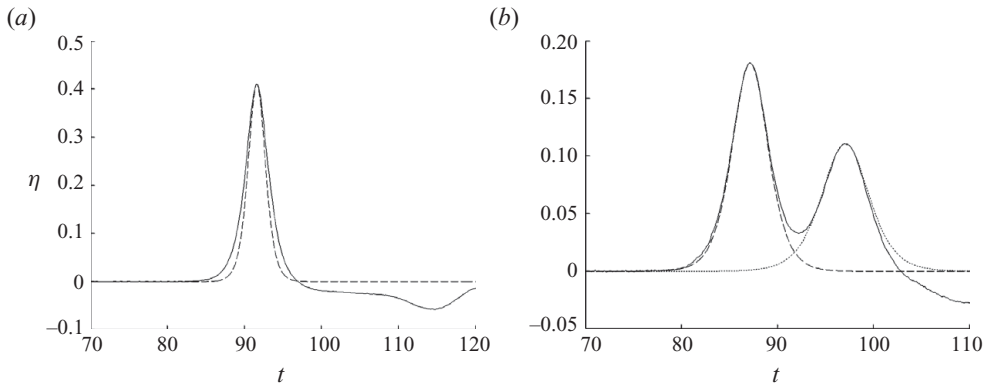
FIGURE 9. Temporal water surface profiles of (*a*) the stem wave at $y = 0.21$ and (*b*) the incident and reflected waves offshore at $y = 12.5$, measured at $x = 71.1$ for the wave shown in figure 7. The dashed and dotted lines represent the profiles of KdV solitons.

To examine the depression behind the Mach stem closely, figure 10 shows the evolution of water-surface profiles at the locations $x = 10.2, 30.5, 50.8$ and 71.1. The figures in the left column show the profiles in the y–t plane, and the middle and right columns are the temporal profiles at the wall ($y = 0.21$) and offshore ($y = 12.5$), respectively. Where x is small ($x = 10.2$, figure 10*a*), there is a compact dip in the trailing portion of the stem wave that is almost negligible in the offshore profile behind the reflected wave. The small dip could have been generated by the wavemaker motion based on the KdV soliton approximation as discussed in figure 4. However, the depression behind the stem wave is significantly more prominent (2.4 mm ($\Delta\eta \approx 0.04$)) than the dispersive trailing dip shown in figure 4 (0.24 mm ($\Delta\eta \approx 0.004$)). Furthermore, such a small and short wave disturbance should have dispersed behind the primary wave and become less apparent downstream, contrary to the results shown in figure 10. A careful examination of figure 10 reveals that the depression becomes elongated as the wave propagates downstream. The depressed water level does not return to the still water level behind the stem, but sustains its set-down of approximately 2 mm ($\Delta\eta \approx 0.033$). The evolution of the depression in fact appears like a wake formation when an object commences in motion. As discussed later in figure 11, the stem and reflected wave amplitudes grow continuously even at $x = 71.1$. This wake-like formation of the depression behind the stem wave must be related to the transient process associated with stem-wave development.

Consider a control volume, bounded by control surfaces sufficiently ahead of and behind the stem wave, moving along the wall with the constant speed $c^* = c_i \sec \psi_i$, where c_i is the phase speed of the incident wave. The net momentum within the control volume increases with time owing to the growth of stem and reflected waves (see figure 11). Hence, the momentum flux through the control surface ahead of the stem wave must be greater than that through the trailing control surface. Since the flow velocities across both control surfaces are the same – the speed c^* in the moving coordinate system – the flow depth must be smaller across the trailing control surface than across the surface ahead of the stem wave. (Note that, in the offshore region where only the incident soliton is present and the reflected wave has not yet been developed, the control surface can be chosen conveniently by aligning the surface tangential to the velocity vectors of the incident line soliton, which results in nil momentum flux across this offshore control surface.) Consequently, the depression
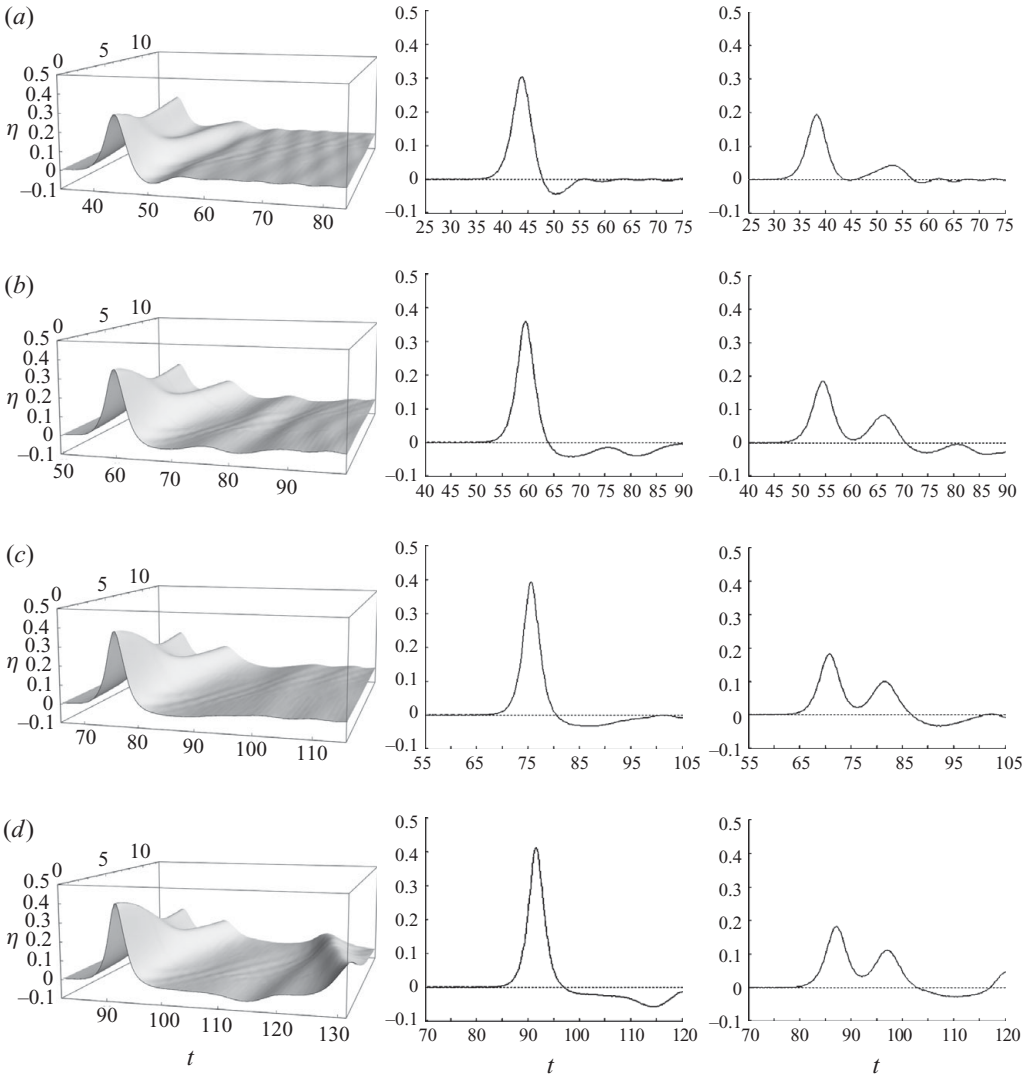
FIGURE 10. Water-surface profiles behind the Mach reflection for the incident wave amplitude $a_i = 0.188$ and the angle $\psi_i = 30°$ ($\kappa = 0.888$): (a) $x = 10.2$; (b) $x = 30.5$; (c) $x = 50.8$; (d) $x = 71.1$. Left: the profiles in the y–t plane; middle and right: the temporal profiles at the wall ($y = 0.21$) and offshore ($y = 12.5$), respectively. Note that the large disturbance that appears near the end of (d), $t > 120$, was caused by the exit reflection when the wave was released from the confined domain of the present experimental set-up (see figure 3a).

behind the stem wave is formed by this transient behaviour associated with the momentum growth within the control volume due to the development of the Mach stem. Growing amplitude means that the stem wave is not a KdV soliton throughout the extent of the experiment. We found that the observed stem wave propagates (6 %–14 %) faster than the KdV soliton with the same amplitude; hence, the observed stem wave is a forced wave.

Another feature seen in figure 10 is the disturbance created when the Mach stem exits from the experimental domain, as seen in figure 10(d) for $x = 71.1$. When the wave escapes from the linearly contracted domain (see our laboratory set-up in
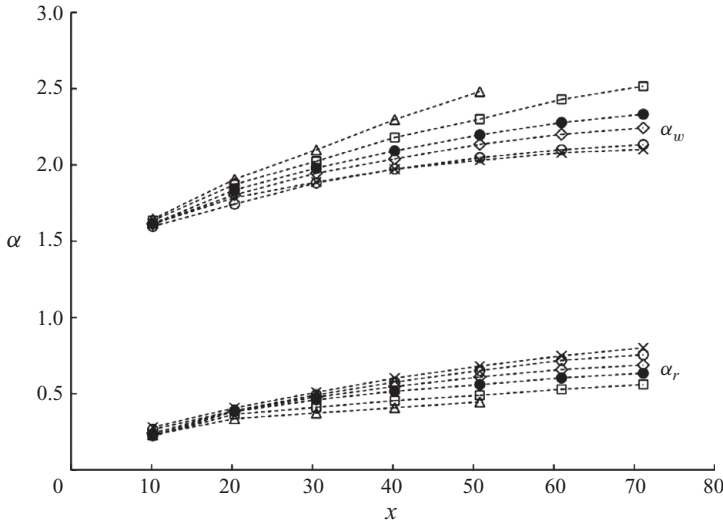
FIGURE 11. Amplification growth of the stem wave α_w and the reflected wave α_r for $\psi_i = 30°$, $h_0 = 6$ cm, and -- × --, $a_i = 0.076$ ($\kappa = 1.395$); -- ○ --, $a_i = 0.096$ ($\kappa = 1.242$); -- ◇ --, $a_i = 0.143$ ($\kappa = 1.020$); -- ● --, $a_i = 0.188$ ($\kappa = 0.888$); -- □ --, $a_i = 0.277$ ($\kappa = 0.731$); -- △ --, $a_i = 0.367$ ($\kappa = 0.636$).

figure 3a), a sudden expansion occurs to the wave at the narrow exit. This creates a disturbance – resembling a partial wave reflection – propagating back to the experimental domain.

Figure 10 also shows the immature reflected wave at $x = 10.2$, having an asymmetrical waveform, decreasing wave amplitude in the offshore direction even at $y = 12.5$, and separating father away from the incident wave. Recall that data of Melville (1980) were taken at a similar location, $x = 16.7$. A smaller wave is shedding out from the reflected wave in the profile at $x = 30.5$ (figure 10b). When x is small (say, $x < 30$), the reflected wave must be in the transient process of its creation and also contaminated by the disturbance that might be generated at $x = 0$ and $y = 0$, where the boundary angle is discontinuous (see figures 1a and 3a).

4.2. *Wave evolution*

Growing stem-wave amplifications α_w ($= a_w/a_i$) induced by incident waves with amplitudes $0.076 \leqslant a_i \leqslant 0.367$ and $\psi_i = 30°$ are presented in figure 11. Also shown is the growth of reflected waves. The stem amplification continues to grow in the cases of larger-amplitude waves. On the other hand, the amplitude tends to approach its equilibrium value for smaller amplitude cases. The reflected wave amplitude also grows. Contrary to the behaviour of stem waves, the larger the incident waves are, the slower the growth of the reflected waves. The amplitude ratio of the reflected wave to the incident wave tends to approach unity ($\alpha_r \rightarrow 1$) for the smaller incident waves. Nevertheless, the limited physical dimension of the laboratory apparatus prevents the stem formation from reaching its fully developed asymptotic state. Note that in figure 11, no complete data are presented for the case of $a_i = 0.367$ because of wave breaking after $x = 50.8$.

Recall that Miles's predictions (1.1)–(1.6) are for the equilibrium state (see figure 1b), whereas the wave reflection observed in the laboratory is in the development process (see figure 1a). Hence, it is difficult to directly compare our laboratory results with

the theory. To remedy this, the evolution is numerically calculated based on the KP equation (2.1), details of the numerical algorithm are presented in the Appendix. Note that the asymptotic solution to the KP equation is equivalent to the theory by Miles (1977*b*), as demonstrated in the Appendix (also by Kodama *et al.* 2009) because the limits and assumptions involved are the same.

The growth process of the stem-wave amplification is presented in figure 12 for cases with amplitudes $0.076 \leqslant a_i \leqslant 0.367$ and $\psi_i = 30°$. As discussed earlier, in order to observe stem-wave amplification at locations farther than the distance available in the wave tank, the extended experimental run was performed by reproducing the waveform measured at $x = 71.1$ with the wavemaker system. By patching the data, this procedure allows us to study wave evolution in an effectively longer wave tank. The data in figure 12 include the amplification at the extended locations $x = 96.6$ and 121.1. (There is no extended data for the case $a_i = 0.367$, because the stem wave breaks after $x = 50.8$ as mentioned earlier.) Also plotted are the numerical predictions from the KP theory as well as the asymptotic values obtained from (1.2). The KP predictions were calculated with the incident wave amplitude a_i measured at $x = 10.2$.

Slight discrepancies that appear in the figure could be attributed to wave attenuation in the laboratory due to viscous effect. For a given incident wave angle ψ_i (in the present cases $\psi_i = 30°$), the interaction parameter κ gradually increases as the incident wave attenuates. This implies that the predicted amplification decreases if $\kappa > 1.0$, and increases if $\kappa < 1.0$ according to (1.2). Although the theoretical prediction (1.2) is for the asymptotic state, the results for $\kappa > 1.0$ shown in figure 12 reflect this trend; the amplification growth is slower than the KP prediction. Contrary to what we expect however, the observed growth rates for $\kappa < 1.0$ are also slower than the prediction except in the case with the smallest κ (or $a_i = 0.367$); figure 12(*f*) shows that the measured growth matches very well with the KP prediction.

It is emphasized that reproducing the 2D wave condition measured at $x = 71.1$ for the extended experiment is not trivial, and we anticipate some error associated with this procedure. In spite of the patchwork of data, the amplifications at the extended locations result in good agreement with the numerical predictions of the KP theory, although they are slightly deviated from the extrapolated trajectory from the parent experiments (up to $x = 71.1$). Figure 12 shows that the growth in amplification from $x = 96.1$ to 121.1 (at the extended locations) is minute for all cases. For the cases of figure 12(*a, b, e*) ($a_i = 0.076$, 0.096 and 0.277), the amplifications reach close to their asymptotic states at $x = 121.1$; for the case of $a_i = 0.367$ (figure 12*f*), it has already reached close to the asymptote at $x = 50.8$ prior to wave breaking. As shown in table 1, the measured stem-wave amplifications are more than 90 % of the asymptotic values. That is not the case for figures 12(*c*) and 12(*d*) ($a_i = 0.143$ and 0.188); they are approximately 75 % of the asymptotic values. These two cases are close to the critical condition $\kappa \sim 1.0$, and our numerical computation indicates that the distance to reach its equilibrium is much longer than other cases (see table 1). On the other hand, the laboratory data in figures 12(*c*) and 12(*d*) show no growth in amplification between $x = 96.1$ and 121.1. The growth pattern in the parent experimental run (the data up to $x = 71, 1$) also indicates reduction of the amplification growth. It appears that the amplification process in the laboratory must be saturated for the cases of figures 12(*c*) and 12(*d*), while further continuous growth was predicted by the numerical prediction.

Measured stem-wave amplifications are plotted in figure 13 with Miles's asymptotic solution (1.2) and Tanaka's numerical results (1993). Note that Tanaka's model is
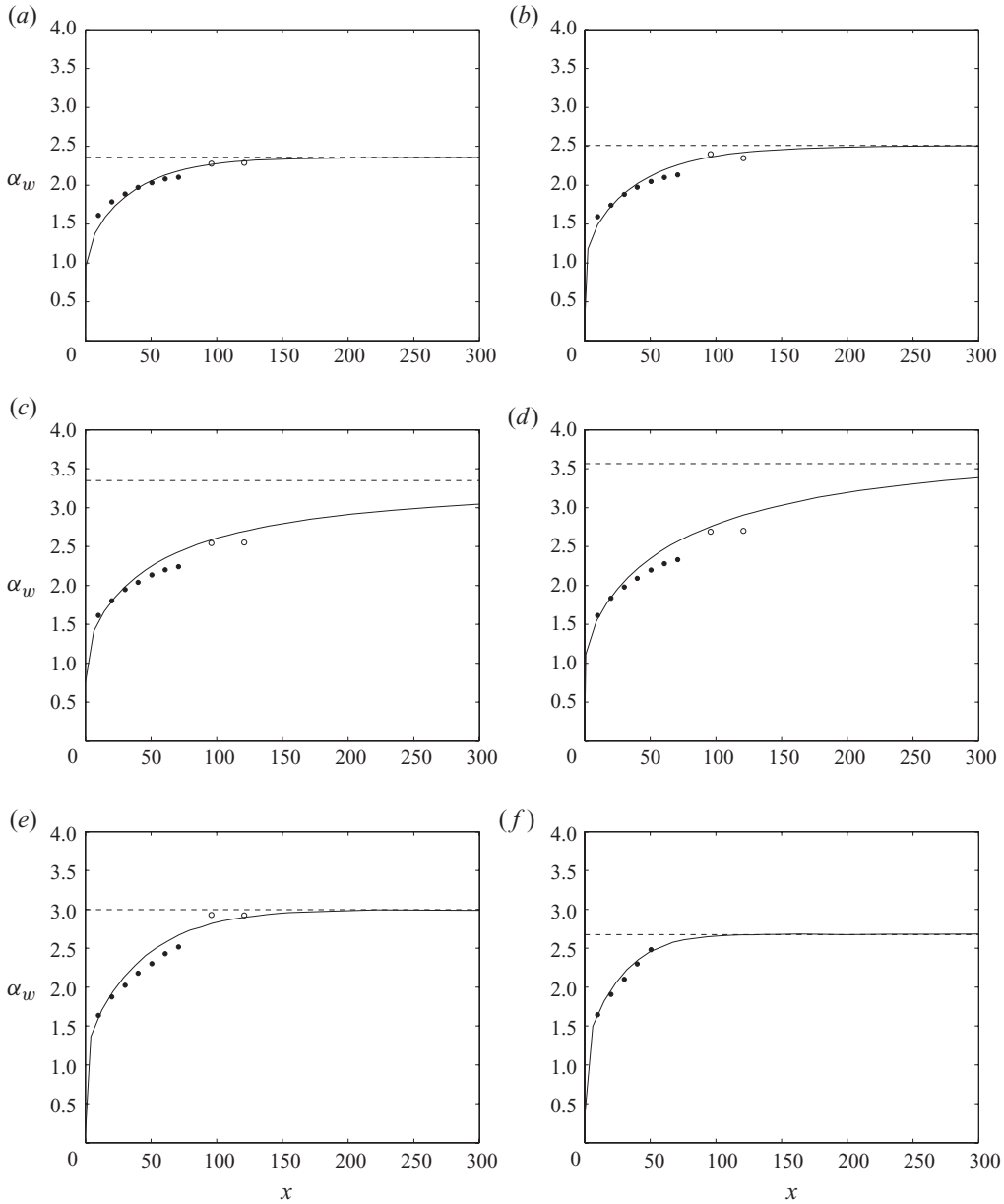
FIGURE 12. Growth of the stem-wave amplification for the cases with $\psi_i = 30°$ and $h_0 = 6$ cm. (a) $a_i = 0.076$, $\kappa = 1.395$; (b) $a_i = 0.096$, $\kappa = 1.242$; (c) $a_i = 0.143$, $\kappa = 1.020$; (d) $a_i = 0.188$, $\kappa = 0.888$; (e) $a_i = 0.277$, $\kappa = 0.731$; (f) $a_i = 0.367$, $\kappa = 0.636$. Lines and symbols: ——, numerical prediction of the KP theory; ----, asymptote of the amplification (1.2); ●, laboratory data; ○, extended laboratory data.

based on the higher-order approximation in nonlinear effects, and the simulations were made for waves with $a_i = 0.3$ and a range of incident wave angles $\psi_i = 10°\text{--}60°$. According to Tanaka, his results are asymptotically stable at $x = 150$, except the data point at $\kappa = 0.90$ ($\psi_i = 35°$), in which the convergence to the asymptotic state is very slow – the same behaviour as our KP simulations as shown in table 1 and figure 12.

Cases $a_i (x = 10.2)$	(1.2) $(x \to \infty)$	α_w $\alpha_{x=71.1} \to \alpha_{x=121.1}$ $(\alpha_w/(1.2))$	α_r $\alpha_{x=71.1} \to \alpha_{x=121.1}$	κ $\kappa_{x=10.2} \to \kappa_{x=121.1}$	x to reach 95 % of α_w $(x \to \infty)$ (KP)
0.076	2.357	$2.101 \to 2.287$ (0.970)	$0.801 \to 1.016$	$1.395 \to 1.506$	85.5
0.096	2.511	$2.133 \to 2.346$ (0.934)	$0.755 \to 0.972$	$1.242 \to 1.358$	104.1
0.143	3.348	$2.242 \to 2.551$ (0.761)	$0.688 \to 0.892$	$1.020 \to 1.138$	502.0
0.188	3.565	$2.332 \to 2.700$ (0.758)	$0.634 \to 0.856$	$0.888 \to 1.004$	299.9
0.277	2.996	$2.516 \to 2.922$ (0.975)	$0.561 \to 0.663$	$0.731 \to 0.834$	103.8
0.367	2.676	2.481^* (0.927)	0.446^*	$0.636 \to 0.649^*$	61.7

TABLE 1. Amplification of the stem (α_w) and reflected (α_r) waves at $x = 71.1$ and 121.1 and the range of the interaction parameter κ. Also shown are the asymptotic stem-wave amplification by (1.2) and the distance to travel to attain 95 % of the asymptotic amplification estimated by the numerical calculations of the KP theory. There is no extended data for the case $a_i = 0.367$, because the stem wave breaks after $x = 50.8$ as indicated by the asterisk.
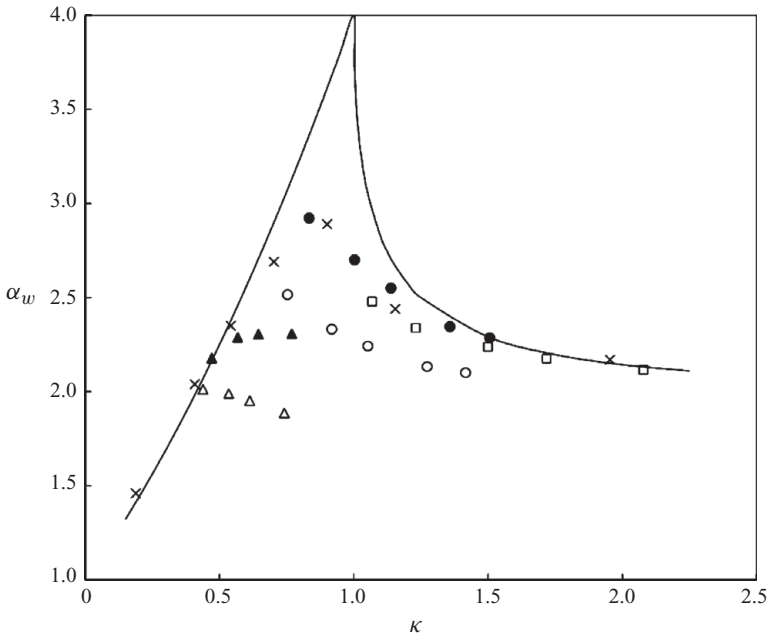

FIGURE 13. Comparison of the stem-wave amplification α_w with the prediction of Miles (1977b) (1.2)(——) and the numerical results of the higher-order model given by Tanaka (1993) ($\times$). The present data are at $x = 71.1$ for $a_i = 0.076$–0.367 and the incident wave angle $\psi_i = 40°$ ($\square$), $\psi_i = 30°$ ($\bigcirc$) and $\psi_i = 20°$ ($\triangle$). The data taken in the extended experimental runs are at $x = 121.1$ with $\psi_i = 30°$ ($\bullet$) and $\psi_i = 20°$ ($\blacktriangle$).

The laboratory results presented in figure 13 include the stem-wave amplification at $x = 71.1$ (our farthest measuring location of the parent experiment) with $\psi_i = 20°$ and 30°, and at $x = 61.0$ with $\psi_i = 40°$; in the case of $\psi_i = 40°$, the data at $x = 71.1$ were contaminated due to flow contraction owing to the limited breadth of the wave tank (see figure 3a). The data obtained at $x = 121.1$ by the extended experimental runs are also presented in the figure; however, no data were taken for the case with $\psi_i = 40°$, because it is difficult for the wavemaker system to reproduce the reflected wave with

the large oblique angle. We consider, however, that the data at $x = 61.0$ for $\psi_i = 40°$ have already reached close to their asymptotic state.

According to figure 13, stem-wave amplifications at $x = 71.1$ show good agreement with the asymptote (1.2) for the case with the incident wave angle $\psi_i = 40°$. However, as the incident wave angle decreases ($\psi_i = 30°$ and $20°$), the measured amplification at $x = 71.1$ (shown by open symbols) deviates from the theoretical prediction. The smaller the incident wave amplitude (or the larger the interaction parameter κ), the smaller the amplification α_w, and for $\kappa < 1.0$ the farther the deviation from (1.2); see the case with $\psi_i = 20°$ shown by the open triangular symbols in figure 13. At the extended location $x = 121.1$ (shown by the filled symbols), the amplification continuously approaches the theoretical prediction of (1.2). In fact, the results with $\psi_i = 30°$ are in excellent agreement with Tanaka's numerical predictions. The results with $\psi_i = 20°$ start to converge the theoretical trend of the Mach reflection for $\kappa < 1.0$, i.e. the amplification increases as κ increases towards its critical value.

As discussed earlier in figure 12, there is little amplification growth between $x = 96.1$ and 121.1 for the case of $\psi_i = 30°$, which means that the wave reflection process became stable. The present laboratory data are in excellent agreement with Tanaka's numerical predictions for, say, $\kappa > 0.8$. The discrepancy in the case of $\psi_i = 20°$ remains due to the limitation in propagation distance in the laboratory; however, the data clearly exhibit approaching the asymptotic state. With a small incidence angle, the stem wave of the Mach reflection continuously grows. We found that the crest length of the stem formation at distant locations becomes too long to reproduce in the limited breadth of our laboratory tank by the wavemaker, which disallows us to perform additional extended experiments beyond $x = 121.1$.

In short, our laboratory results tend to approach numerical results of Tanaka (1993). Furthermore, when κ is away from unity, the present laboratory results support the theoretical prediction (1.2). Note that Tanaka provided his data for the cases with only one incident-wave amplitude $a_i = 0.3$, while our laboratory results are based on a variety of wave amplitudes a_i as well as the three incident wave angles. Good agreement with Tanaka's results implies that smaller amplification than (1.2) for the data near $\kappa = 1.0$ (for example, the results shown in figures 12c and 12d) is probably attributable to the higher-order nonlinearity effects.

Figure 14 shows the wave profiles taken with the LIF method at $x = 71.1$, 96.1 and 121.1 with $\psi_i = 30°$ for three cases: (a) $a_i = 0.076$, (b) 0.188 and (c) 0.277. Note that the first panel of figure 14(b) is identical to figure 7. The profiles at $x = 71.1$ are obtained from the parent experiments by generating the prescribed incident line soliton, while the profiles at $x = 96.1$ and 121.1 are obtained by the foregoing extended experiments by reproducing the waveform (including the stem and reflected waves) observed at $x = 71.1$. Some noises (horizontal strips) that appear in the profiles are related to the overlapping LIF images in the montage process. Visual observations provide a justification for our patching procedure to create the effectively longer propagation distance; the waveforms in figure 14 are essentially consistent. The three cases (figure 14a–c) exhibit different evolution patterns in the profiles. The Y-shaped profile of case (a) ($a_i = 0.076$) shows little change as it propagates from $x = 71.1$ to 121.1, whereas the stem length is clearly growing for case (c) ($a_i = 0.277$). This behaviour is consistent with the theoretical prediction; continuous growth of the stem angle ψ_w when $\kappa < 1$ (for case (c), $\kappa = 0.834$ at $x = 121.1$, $\kappa = 0.731$ at $x = 10.2$), and no growth for regular reflection when $\kappa > 1$. The stem length shown in figure 14(a) ($\kappa = 1.506$ at $x = 121.1$, $\kappa = 1.395$ at $x = 10.2$) maintains its forms with constant length. For this case, the amplification of the reflected wave is $\alpha_r = 1.016$ at $x = 121.1$
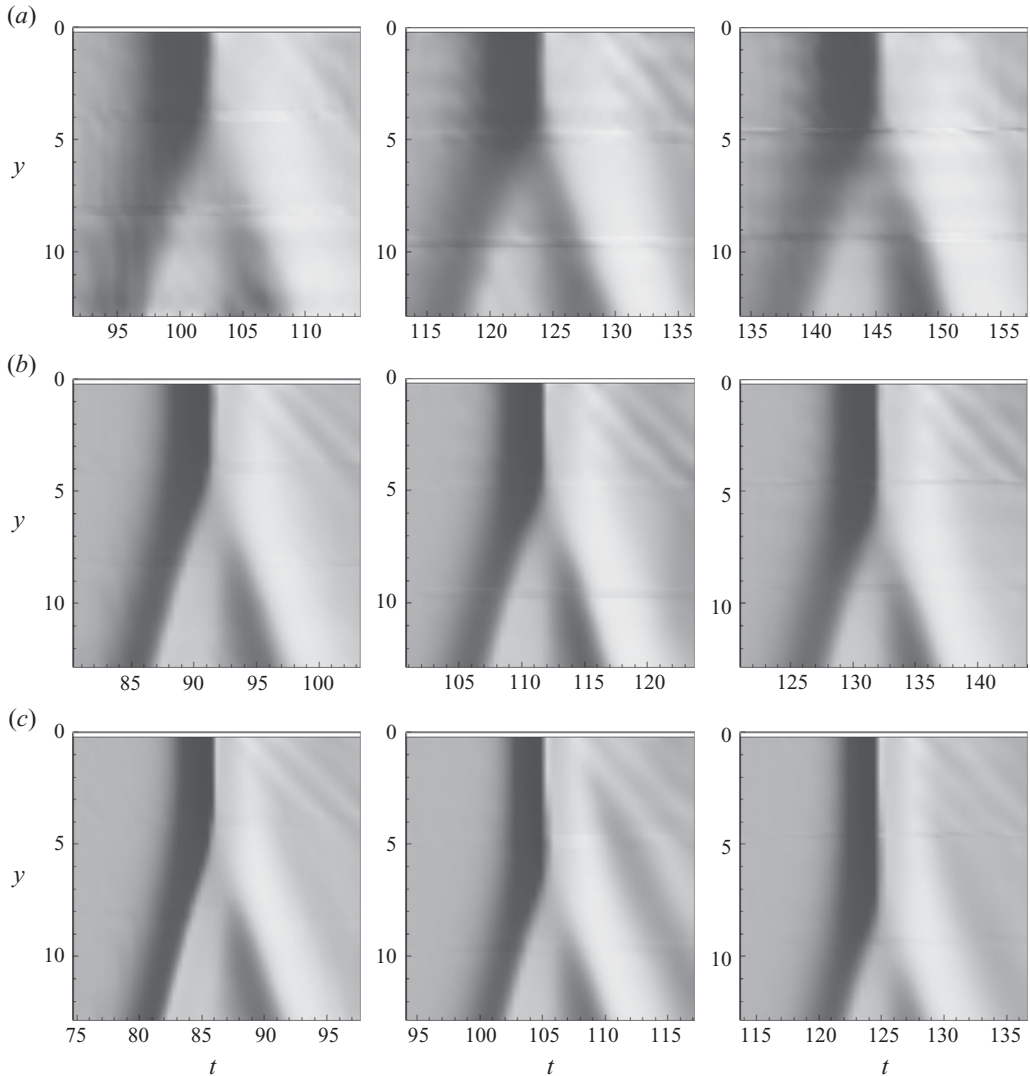
FIGURE 14. Evolution of the water-surface profiles at $x = 71.1$ (left), 96.1 (centre) and 121.1 (right) for the incident waves: (a) $a_i = 0.076$ ($\kappa = 1.395$), (b) $a_i = 0.188$ ($\kappa = 0.888$) and (c) $a_i = 0.277$ ($\kappa = 0.731$). The wall is located at $y = 0$, the water depth $h_0 = 6.0$ cm, and the incident wave angle $\psi_i = 30°$. The data were obtained by the LIF method with the vertical laser sheet along the y-direction.

as indicated in table 1, and the measured reflected wave angle is $\psi_r = 32.6°$, very close to the incident wave angle – these are the characteristics of regular reflection. This stem wave formation of regular reflection does not seem to disappear for further propagation, considering the conditions of $\alpha_r = 1.0$ and $\psi_i = \psi_r$ that should maintain the existing waveform.

Evolution processes of the stem-wave elongation are shown in figure 15 for the cases with $0.076 \leqslant a_i \leqslant 0.367$ and $\psi_i = 30°$. Figure 15(a) shows growth of the stem length, indicating that the larger the amplitude the faster the growth. Figure 15(b) shows the stem-length growth rate ψ_w assuming the linear growth as depicted in
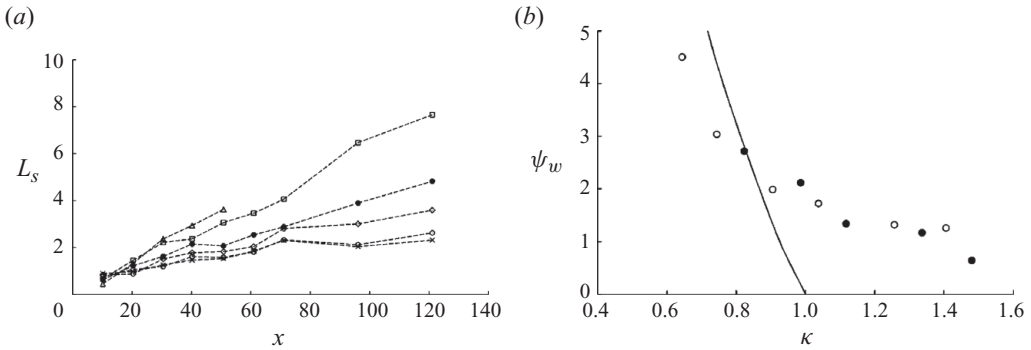
FIGURE 15. The stem length L_s determined by the method depicted in figure 8. (*a*) Growth of the length in x with $\psi_i = 30°$: --×--, $a_i = 0.076$ ($\kappa = 1.395$); -- ○ --, $a_i = 0.096$ ($\kappa = 1.242$); -- ◇ --, $a_i = 0.143$ ($\kappa = 1.020$); -- ● --, $a_i = 0.188$ ($\kappa = 0.888$); -- □ --, $a_i = 0.277$ ($\kappa = 0.731$); -- △ --, $a_i = 0.367$ ($\kappa = 0.636$); and (*b*) the stem wave growth angle ψ_w (in degrees) up to $x = 71.1$ (○); the angle ψ_w between $x = 96.1$ and 121.1 (●); prediction (1.6) (——).

figure 1. The stem lengths are determined by the method presented in figure 8. As seen in figure 15(*a*), cases of $a_i = 0.076$ and 0.096 almost cease the stem-length growth at $x > 71.1$, whereas those of $a_i = 0.188$ and 0.277 appear to grow continuously at linear rates. According to figure 13, cases $a_i = 0.076$ and 0.096 (the rightmost filled circular symbols in figure 13) reach their asymptotic state of regular reflection. While the stem-length growth has ceased, the length remains finite after the stem is formed during the development of the reflection. For cases $a_i = 0.188$ and 0.277 (the leftmost filled circular symbol in figure 13), the stem length is still continuously growing in accordance with the behaviour of the Mach reflection for $\kappa < 1.0$. As shown in table 1, $\kappa \leqslant 1.004$ and $\leqslant 0.834$ for cases $a_i = 0.188$ and 0.277, respectively – note that the value of κ increases as the wave propagates due to slow attenuation of the incident wave.

Using linear regression on the measured data in figure 15(*a*), the growth rates are determined and plotted with Miles's prediction (1.6) in figure 15(*b*). In the figure, the open symbols represent the linear growth rates based on the data up to $x = 71.1$, i.e. the parent experimental runs, while the solid symbols show the rates between $x = 96.1$ and 121.1 of the extended experimental runs. Despite the potential error associated with our patching procedure, the results in figure 15(*b*) show that the two sets of data are consistent, demonstrating the validity of our patching procedure to obtain data equivalent to an effectively long wave tank. Although the trend of the data shown in figure 15(*b*) is similar to (1.6), no sharp transition at $\kappa = 1.0$ is observed in the laboratory data.

Figure 16 shows the characteristics of the reflected waves; the amplitudes and the angles are presented in figures 16(*a*) and 16(*b*), respectively. The laboratory data at $x = 121.1$ are in good agreement with Miles's predictions (1.4) and (1.5) as well as Tanaka's numerical prediction. Note that the reflected wave amplitudes at $x = 71.1$ (the farthest measurement location for the parent experimental runs) still show their developing stages. It is emphasized that Tanaka's numerical results were for a single incident wave amplitude, $a_i = 0.30$ with a range of the incident wave angle $\psi_i = 10°$–$60°$, whereas the present laboratory results shown in figure 16 are based on the single incident wave angle $\psi_i = 30°$ with a range of incident wave amplitudes $a_i = 0.076$–0.277. Considering the different experimental parameters, the agreement in the reflected waves in figure 16 is remarkable. It must be pointed out that Tanaka's
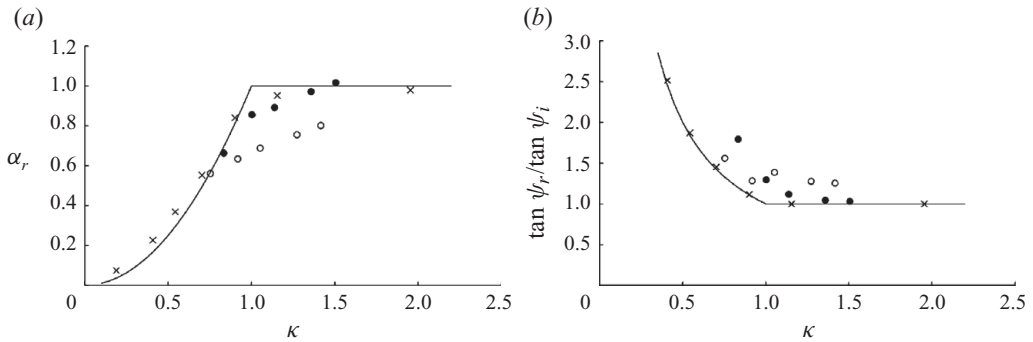
(*a*)   (*b*)

FIGURE 16. Evolution of reflected waves: (*a*) reflected-wave amplification α_r and (*b*) reflected wave angle ψ_r at $x = 71.1$ ($\bigcirc$); $x = 121.1$ ($\bullet$); Tanaka's (1993) numerical data, $\times$. The solid line in (*a*) is Miles's theoretical prediction (1.4), and the solid line in (*b*) is (1.5).

numerical results of the reflected wave angles now appear to be in near-perfect agreement with (1.5) as shown in figure 16(*b*), which evidently resulted from correct use of the interpreted interaction parameter κ presented in (2.10), instead of the original parameter k in (1.3).

4.3. *Wave breaking*

Recall that no data were presented beyond $x = 50.8$ for the case of $a_i = 0.367$ in figures 11 and 12 because of the occurrence of wave breaking. Figure 17 shows the temporal variation of breaking waves along the wall at $x = 61.0$ and the incident wave angle $\psi_i = 30°$. The wave profile was captured every 0.01 s using the LIF method of aligning the laser sheet parallel to the wall. Three panels in the figure were made from data at the same location but slightly different in the incident wave amplitude ($a_i = 0.351, 0.359, 0.367$ at $x = 10.2$). Gradual but continuous growth in wave amplitude can be seen prior to the incipience of wave breaking in figure 17(*a*). The maximum wave height a_w at the wall reaches 0.910, just at the incipience of the breaking. This wave height is higher than the maximum solitary wave height of 0.827 (Longuet-Higgins & Fenton 1974). Numerical simulation of Tanaka (1993) also achieved a maximum amplitude higher than 0.827; he found $a_w = 0.905$ at $x = 150$ when $a_i = 0.3$ and $\psi_i = 20°$. Our experimental results in figure 17 confirm that the Mach stem height can become higher than the highest plain solitary wave. Figures 17(*b*) and 17(*c*) show the evolution of the wave breaking. The vertical-step-like appearance on the wavefront is the portion of overturning wave; our LIF cannot capture the detailed features of the overturning motion because of blockage of the laser light by the overturning tongue of water. Very short spatial oscillations in front of the overturning water are capillary waves running down the steep front slope. While the overturning portion increases, the wave amplitude gradually decreases, as seen in figures 17(*b*) and 17(*c*).

Figure 18 shows the breaking wave profiles at $x = 61.0$ and 71.1 for the case $a_i = 0.367$ (the same wave as shown in figure 17*c*). Several features that appear in the figure are worth noting. First, breaking starts near the wall and broadens towards offshore. While the wave amplitude decreases near the wall due to energy dissipation, the amplitude continues to grow in the area away from the wall. The maximum wave amplitude at $x = 71.1$ is $a = 0.856$ at $y = 3.17$. At the same offshore location ($y = 3.17$) but at $x = 61.0$, the amplitude is $a = 0.758$; that is 13 % growth from $x = 61.0$ to 71.1. This growth rate is substantially faster than the growth rate of the
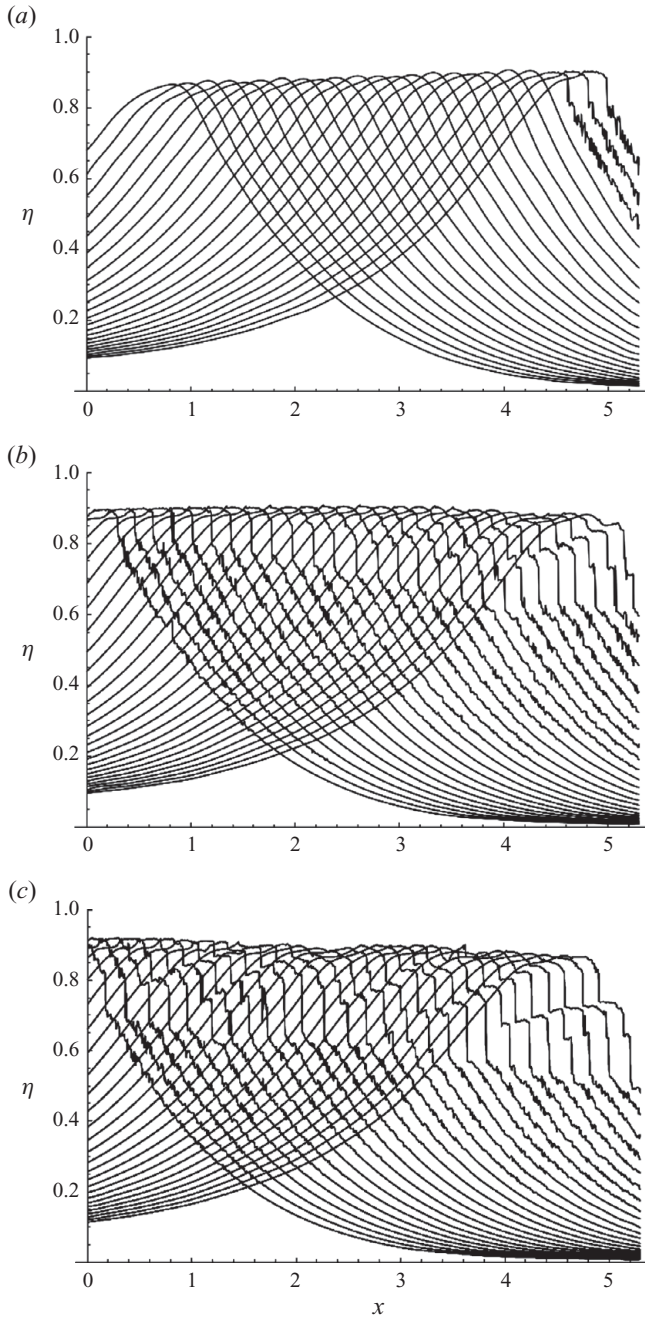
FIGURE 17. Temporal variation of the stem-wave profile at the incipient breaking along the wall at $x = 61.0$ with $\psi_i = 30°$, $h_0 = 6$ cm and $\Delta t = 0.01$ s: (a) $a_i = 0.351$, (b) $a_i = 0.359$, (c) $a_i = 0.367$.

Mach stem prior to wave breaking. Prior to wave breaking, figure 11 shows a 6.9 % increase in amplitude from $x = 40.2$ to 50.8 at the wall. Perhaps more important, the water-surface slope facing the y-direction is substantially steeper at $x = 71.1$ than at $x = 61.0$. This amplitude growth cannot be explained with the growth of the stem
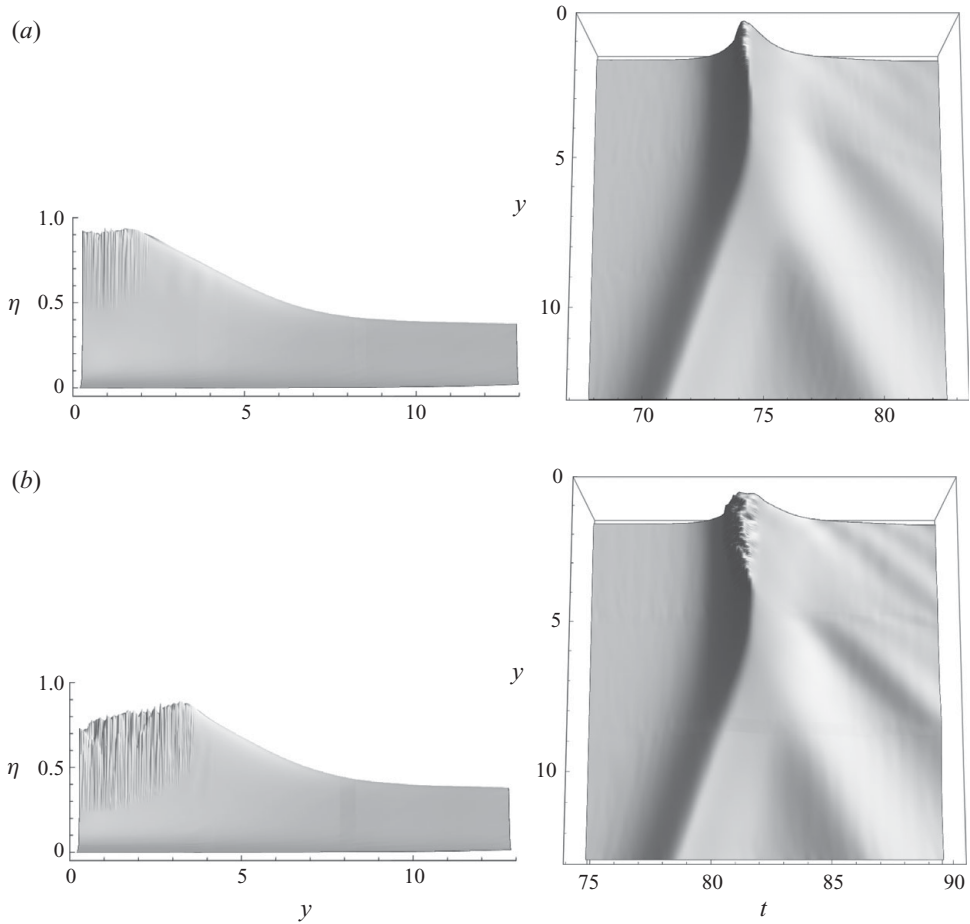
FIGURE 18. Wave-breaking profiles of the Mach stem for the case of $a_i = 0.367$ with $\psi_i = 30°$ and $h_0 = 6$ cm: (a) at $x = 61.0$ and (b) $x = 71.1$. The elevation views from the horizontal x-direction (left) and plan views from the top (right).

length alone. One explanation for the faster increase in amplitude offshore is the increase in momentum in the y-direction near the wall due to turbulence induced by wave breaking.

Figure 18(b) shows how the wave breaking deforms its wave crest forward and results in the bow-like wave formation near the wall. The wave crest at $x = 71.1$ is broader than that at $x = 61.0$. The crest shape at $x = 61.0$ is still peaked, even just after the incipience of wave breaking, but it transforms to a bore-like (broken wave) state at $x = 71.1$. Also observed is the substantial trailing disturbance caused by wave breaking, resulting in a much rougher water surface behind the stem wave.

5. Summary and conclusions

Laboratory experiments were performed to examine reflection of a solitary wave at a vertically placed wall with an oblique incident-wave angle. Measurements of water-surface variations in sub-millimetre precision were achieved using the LIF method. Results are analysed with previous theoretical prediction of Miles (1977b), a laboratory

study of Melville (1980) and numerical results by Tanaka (1993). Miles's model is based on resonant triad interaction of three KdV solitons that yield the asymptotic conditions of the wave reflection; his theory is for the lowest-order nonlinear and dispersive shallow-water waves with the assumption of quasi-two-dimensionality, i.e. very small oblique angle. Tanaka's numerical simulations are based on a spectral model for higher-order nonlinear and dispersive shallow-water waves.

When the theory is validated with either numerical or laboratory experiments, we found that the interaction parameter κ of the form of (2.10) must be used instead of the original form of (1.3), k. This is because an oblique angle of the incident wave is not infinitesimal, but finite in real-world experiments. With the use of (2.10), the previous numerical results given by Tanaka (1993) are in much better agreement with Miles's theoretical predictions than what Tanaka reported in his paper.

We experimentally verified the Mach reflection formation characterized by (i) the Y-shape formation of the incident, reflected and stem waves; (ii) the reflected wave angle being larger than the incident wave angle, $\psi_r > \psi_i$; (iii) the amplitude of the reflected wave being smaller than the incident wave, $a_r < a_i$, and the stem-wave amplitude being larger than the incident wave, $a_w > a_i$; and (iv) the crest of the stem wave being continuously elongated as it propagates along the wall, $\psi_w > 0$. Contrary to the assumption of the theory by Miles (1977b), our observations indicate that during the development stage the stem wave is not a KdV soliton; the measured profile is broader and propagation speed is faster. The stem wave appears to be a forced wave instead of a free soliton. Evidently, Miles's assumption is only valid for the asymptotic state, but not during its development process observed in the laboratory. Furthermore, substantial depression (or setdown) in water level is formed behind the stem wave. This depression is initially a compact dip formation; then it becomes broadened as the wave propagates along the wall. Its magnitude and evolution behaviour differ from the dispersive-wave noise that arises from the wave generation that is programmed for the solitary waves. The transient process of stem-wave development must be responsible for the trailing depression formation. A growing stem wave increases the momentum; hence, the momentum flux ahead of the stem wave must be greater than behind it. Consequently, the water depth has to be lower behind the stem wave. No such depression formation is predicted by Miles's theory because the theory assumes the equilibrium state.

Because Miles's theory is limited to the asymptotic state, the evolution process of the stem-wave development is numerically calculated based on the KP equation. To examine the evolution in an effectively longer distance than the limited size of the laboratory apparatus, we use a technique linking two separate experiments and patch the data. This can be achieved by generating the waveform measured at the farthest location, and observing the subsequent evolution of the generated waveform.

It was found that the stem-wave amplification is in good agreement with the numerical KP prediction. The laboratory results are also in good agreement with the asymptotic state of Miles's theory (1.2) when the value of the interaction parameter κ is not close to the critical value of unity. When $\kappa \approx 1$, the KP theory predicts slow but continuous growth of the amplification, while the laboratory data indicate cessation of growth. While the measured maximum amplification is smaller than Miles's theoretical prediction in the neighbourhood of $\kappa \approx 1$, it was found to be in excellent agreement with the numerical results of Tanaka (1993). The critical fourfold amplification predicted by (1.2) was not realized in the real-fluid environment or in the finite-amplitude numerical simulations. Note that the derivative of (1.2) becomes singular as κ decreases towards unity, although the derivative is finite ($= 4$) as κ

increases towards unity. Evidently, when $\kappa \approx 1.0^{+}$, a small change in κ causes a substantial change in amplification. It appears that the fourfold amplification at the critical condition of $\kappa = 1.0$ is extremely sensitive. It is conjectured based on the present results (e.g. figures 13, 15 and 16) that the transition between the Mach reflection and the regular reflection be gradual, instead of the abrupt change at $\kappa = 1.0$, and the maximum amplification must be lower $\alpha_w < 4$ due to the higher-order nonlinearity effect.

The measured wave profiles show the distinctive differences of Mach reflection from regular reflection as predicted by Miles's theory (1977b), although the transition between those two reflection patterns is not abrupt, but gradual in the laboratory. For example, the experimental cases with $\kappa < 1.0$ show continuous growth in the stem-wave elongation ($\psi_w > 0$), smaller reflected wave amplitude than that of the incident wave ($\alpha_r < 1$), and greater reflected wave angle than the incident angle ($\psi_r > \psi_i$). On the other hand, the cases with $\kappa > 1.0$ show $\psi_w \to 0$, $\alpha_r \to 1$ and $\psi_r \to \psi_i$; those are the behaviours of regular reflection.

We examined the maximum wave height of the Mach stem prior to its wave breaking and found that the maximum wave height $a_w = 0.910$ exceeds the maximum height $a_w = 0.827$ of the plain solitary wave (Longuet-Higgins & Fenton 1974). This result is in accordance with Tanaka's numerical result (i.e. $a_w = 0.905$). After incipient breaking near the wall, the breaking broadens offshore, shifting the location of the maximum water-surface elevation offshore. The water-surface elevation offshore grows faster. This behaviour must be caused by an enhancement in momentum in the offshore direction near the wall, which must be resulted from turbulence induced by wave breaking.

Lastly, it is emphasized that Tanaka's numerical results are limited to the conditions of $a_i = 0.3$ and $10° \leqslant \psi_i \leqslant 60°$, computed up to $x = 150$. Melville's laboratory experiments were performed with the conditions of $a_i = 0.1$ and 0.15, and $10° \leqslant \psi_i \leqslant 45°$, measured up to $x \leqslant 26.7$. Both studies concluded that substantial discrepancies existed between their results and the theory by Miles (1977b). The present laboratory experiments are based on incident wave amplitudes in the range of $0.076 \leqslant a_i \leqslant 0.367$ with the incident wave angles $20° \leqslant \psi_i \leqslant 40°$. Our farthest measurement location is at $x = 71.1$ in the parent experimental runs and further extended to $x = 121.1$ in the extended experimental runs. The present laboratory experiments are the first to present results supporting Miles's theoretical predictions (1977b), as well as in excellent agreement with Tanaka's numerical results (1993). This success is partly attributed to a physically viable interpretation for the interaction parameter and the use of the modified form κ of (2.10), instead of the original k (1.3).

Appendix. Numerical calculations

The laboratory experiments are numerically simulated based on the KP equation. From the outset, we consider the condition such that η and all its derivatives vanish as $|x| \to \infty$ for any time t. Then, integrating the KP equation (2.1) with respect to x

yields

$$\eta_t + \left(c_0\eta + \frac{3c_0}{4h_0}\eta^2\right)_x + \frac{c_0{h_0}^2}{6}\eta_{xxx} = \int_{-\infty}^{x} -\frac{c_0}{2}\eta_{yy}\,\mathrm{d}x. \qquad (A\,1)$$

The numerical calculations are performed in the dimensional form of (A 1). The computational domain is larger than the laboratory wave tank: $L_x = 60$ m long in the x-direction and $L_y = 4$ m wide in the y-direction for the simulations with $\psi_i = 30°$ and $40°$, while $L_y = 6$ m is used for $\psi_i = 20°$ in order to accommodate its longer stem-wave elongation. Just as our laboratory experiments, the water depth at the quiescent state is $h_0 = 6$ cm.

The fractional step method is applied by splitting (A 1) into three sub-steps:

$$(A)\ \eta_t = -\frac{c_0 h_0^2}{6}\eta_{xxx}, \quad (B)\ \eta_t = -\left(c_0\eta + \frac{3c_0}{4h_0}\eta^2\right)_x, \quad (C)\ \eta_t = \int_{-\infty}^{x} -\frac{c_0}{2}\eta_{yy}\,\mathrm{d}x. \quad (A\,2)$$

In order to obtain the second-order accuracy in time, the modified Strang splitting method is applied (Strang 1968). We compute the sequence of A → B → C in one time step, and then for the subsequent time step, reverse the sequence to C → B → A, and continue this alternating sequence. With the use of Taylor series expansion, it can be shown that this procedure guarantees second-order accuracy in time (LeVeque 2002).

The Crank–Nicolson method is used to solve step (A) with centred finite difference. Step (B) is a typical 1D Riemann problem, which is computed by the Godunov method with the second-order accuracy utilizing the software CLAWPACK (LeVeque 2002), which solves time-dependent nonlinear hyperbolic systems of conservation laws. The computation of step (C) needs some explanations. Considering the imposed condition such that η and all its derivatives vanish $|x| \to \infty$ for any time t, we can set $\eta = 0$ and $\eta_t = 0$ at the rightmost boundary $x = L_x$ that is chosen far enough so that the simulated wave does not reach the boundary during the simulation. This condition yields conveniently

$$\int_{-\infty}^{L_x} -\frac{c_0}{2}\eta_{yy}\,\mathrm{d}x = 0. \qquad (A\,3)$$

Hence,

$$\eta_t = \int_{-\infty}^{x} -\frac{c_0}{2}\eta_{yy}\,\mathrm{d}x = \int_{-\infty}^{x} -\frac{c_0}{2}\eta_{yy}\,\mathrm{d}x - \int_{-\infty}^{L_x} -\frac{c_0}{2}\eta_{yy}\,\mathrm{d}x = \int_{x}^{L_x} \frac{c_0}{2}\eta_{yy}\,\mathrm{d}x. \qquad (A\,4)$$

Equation (A 4) is also computed by the Crank–Nicolson method with centred finite difference.

The grid size for the central finite-difference scheme is $\Delta x = 1$ cm, $\Delta y = \Delta x \cot \psi_r$ in which the reflected wave angle ψ_r is determined by (1.5), and $\Delta t = 0.005$ s. With these choices, the Courant–Friedrichs–Lewy number is 0.46–0.52, depending on the wave amplitudes we simulated.

The boundary condition at $x = 0$ is

$$\eta = a_0 \operatorname{sech}^2 \sqrt{\frac{3a_0}{4h_0^3}} \left[y \tan \psi - c_0 \left(1 + \frac{1}{2}\frac{a_0}{h_0} + \frac{1}{2}\tan^2\psi \right)(t - t_0) \right], \qquad (A\,5)$$

where we use $t_0 = 5\sqrt{4h_0^2/3a_0 g}$ to ensure to yield sufficiently long time, so that $\eta \to 0$ at $x = y = 0$ when $t = 0$. At $y = L_y$, the line soliton is maintained by specifying
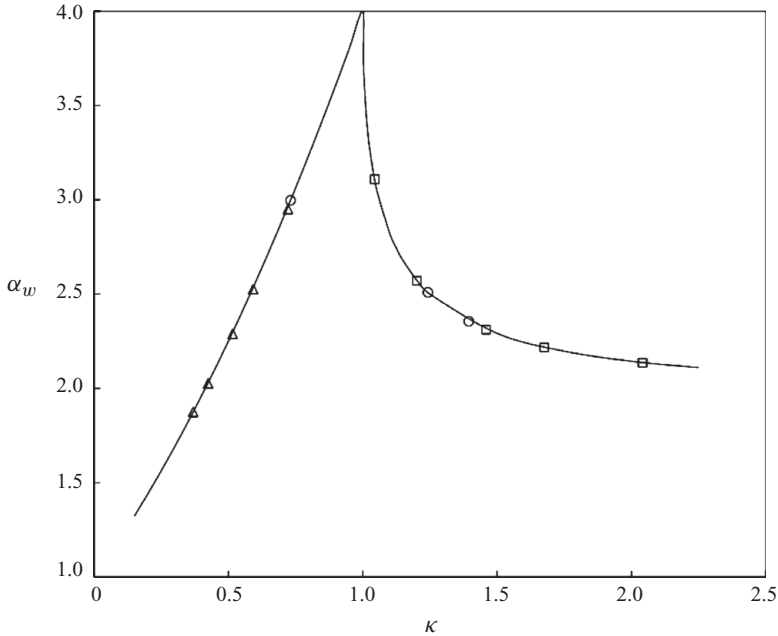
FIGURE 19. The calculated stem-wave amplification at the asymptotic state with the prediction of Miles (1977b) based on the three-wave resonant interaction (1.2), ——; the numerical results are for the wave conditions shown in figure 13, i.e. $a_i = 0.076$–0.367 and the incident wave angle $\psi_i = 40°$ ($\square$), $\psi_i = 30°$ ($\bigcirc$), $\psi_i = 20°$ ($\triangle$).

$\eta\left(y = L_y\right) = \eta_{KP}\left(x, L_y, t\right)$ and $\eta\left(y = L_y - \Delta y\right) = \eta_{KP}\left(x, L_y - \Delta y, t\right)$, where

$$\eta_{KP}(x, y, t) = a_0 \operatorname{sech}^2 \sqrt{\frac{3a_0}{4h_0^3}} \left[x + y \tan\psi - c_0 \left(1 + \frac{1}{2}\frac{a_0}{h_0} + \frac{1}{2}\tan^2\psi \right)(t - t_0) \right].$$
(A 6)

Furthermore, we also specify the reflected wave angle ψ_r at $y = L_y$ with the aforementioned choice of the grid, $\Delta y = \Delta x \cot \psi_r$.

It must be emphasized that as discussed in (2.2)–(2.5), the physical wave amplitude and water-surface elevation need to be retrieved by $\hat{a}_0 = a_0 / \cos^2 \psi_i$ and $\hat{\eta} = \eta / \cos^2 \psi_i$, respectively.

On the basis of the foregoing procedures, the laboratory conditions ($0.076 \leqslant a_i \leqslant 0.367$ with $h_0 = 6$ cm and $\psi_i = 20°$, $30°$ and $40°$) are calculated numerically and the results are presented with the theory of Miles (1977b) in figure 19. The results are in accordance with the theory as anticipated.

REFERENCES

BARAKHNIN, V. B. & KHAKIMZYANOV, G. S. 1999 Numerical simulation of an obliquely incident solitary wave. *J. Appl. Mech. Tech. Phys.* **40**, 1008–1015.

CHAKRAVARTY, C. & KODAMA, Y. 2009 Soliton solutions of the KP equation and application to shallow water waves. *Stud. Appl. Math.* **123**, 83–151.

COURANT, R. & FRIEDRICHS, K. O. 1948 *Supersonic Flow and Shock Waves.* Intersciences.

DIORIO, J. D., LIU, X. & DUNCAN, J. H. 2009 An experimental investigation of incipient spilling breakers. *J. Fluid Mech.* **633**, 271–283.

DUNCAN, J. H., PHILOMIN, V., BEHRES, M. & KIMMEL, J. 1994 The formation of spilling breaking water waves. *Phys. Fluids* **6** (8), 2558–2560.

DUNCAN, J. H., QIAO, H., PHILOMIN, V. & WENZ, A. 1999. Gentle spilling breakers: crest profile evolution. *J. Fluid Mech.* **379**, 191–222.

FUNAKOSHI, M. 1980. Reflection of obliquely incident solitary waves. *J. Phys. Soc. Japan* **49**, 2371–2379.

GARDARSSON, S. M. & YEH, H. 2007 Hysteresis in shallow water sloshing. *J. Engng Mech. ASCE* **133**, 1093–1100.

GORING, D. G. 1979 Tsunami: the propagation of long waves onto a shelf. PhD thesis, California Institute of Technology.

GUIZIEN, K. & BARTHÉLEMY, R. 2002 Accuracy of solitary wave generation by a piston wave maker. *J. Hydraul. Res.* **40**, 321–331.

KATO, S., TAKAGI, T. & KAWAHARA, M. 1998 A finite element analysis of Mach reflection by using the Boussinesq equation. *Intl J. Numer. Meth. Fluids* **28**, 617–631.

KODAMA, Y., OIKAWA, M. & TSUJI, H. 2009 Soliton solutions of the KP equation with V-shape initial waves. *J. Phys. A: Math. Theor.* **42**, 1–9.

LEVEQUE, R. J. 2002 *Finite Volume Methods for Hyperbolic Problems*. Cambridge University Press.

LIU, X. & DUNCAN, J. H. 2006 An experimental study of surfactant effects on spilling breakers. *J. Fluid Mech.* **567**, 433–455.

LONGUET-HIGGINS, M. S. & FENTON, J. D. 1974 On the mass, momentum, energy and circulation of a solitary wave. II. *Proc. R. Soc. Lond.* A **340**, 471–493.

MELVILLE, W. K. 1980 On the Mach reflexion of a solitary wave. *J. Fluid Mech.* **98**, 285–297.

MILES, J. W. 1977a Obliquely interacting solitary waves. *J. Fluid Mech.* **79**, 157–169.

MILES, J. W. 1977b Resonantly interacting solitary waves. *J. Fluid Mech.* **79**, 171–179.

VON NEUMANN, J. 1943 Oblique reflection of shocks. *Explosives Research Rep.* 12. Navy Department, Bureau of Ordnance, Washington, DC. (Also in *John von Neumann Collected Works* (ed. A. H. Taub), vol. 6, pp. 238–299, MacMillan, 1963.)

PERROUD, P. H. 1957 The solitary wave reflection along a straight vertical wall at oblique incidence. *Tech. Rep.* 99/3. University of California, Berkeley.

RAMSDEN, J. D. 1993 Tsunamis: forces on a vertical wall caused by long waves, bores, and surges on a dry bed. PhD thesis, California Institute of Technology.

TANAKA, M. 1993 Mach reflection of a large-amplitude solitary wave. *J. Fluid Mech.* **248**, 637–661.

STRANG, G. 1968 On the construction and comparison of difference schemes. *SIAM J. Numer. Anal.* **5** (3), 506–517.

WHITHAM, G. B. 1974 *Linear and Nonlinear Waves*. Wiley-Interscience.

YEH, H. & GHAZALI, A. 1986 A bore on a uniformly sloping beach. In *Proc. 20th Intl Conf. on Coastal Engineering*, pp. 877–888.

YEH, H., LI, W. & KODAMA, Y. 2010 Mach reflection and KP solitons in shallow water. *Eur. Phys. J. Special Topics* **185**, 97–111.